ACOUSTIC EMISSION EVALUATION AND MECHANICAL PROPERTY CHARACTERIZATION OF STAINLESS STEEL SPECIMENS MANUFACTURED BY POWDER BASED 3-D PRINTER

by

Yongsen Rong

B.S, Wuhan University, 2013

Submitted to the Graduate Faculty of

Swanson School of Engineering in partial fulfillment

of the requirements for the degree of

Master of Science

University of Pittsburgh

2015

UNIVERSITY OF PITTSBURGH

SWANSON SCHOOL OF ENGINEERING

This thesis was presented

by

Yongsen Rong

It was defended on

April 1st, 2015

and approved by

Qing-Ming Wang, PhD, Professor

Department of Mechanical Engineering and Materials Science

C. Isaac Garcia, PhD, Research Professor

Department of Mechanical Engineering and Materials Science

Ian Nettleship, PhD, Associate Professor

Thesis Advisor: Qing-Ming Wang, PhD, Professor

Department of Mechanical Engineering and Materials Science

ACOUSTIC EMISSION EVALUATION AND MECHANICAL PROPERTY CHARACTERIZATION OF STAINLESS STEEL SPECIMENS MANUFACTURED BY POWDER BASED 3-D PRINTER

Yongsen Rong, M.S.

University of Pittsburgh, 2015

This research aims at establishing relationship between acoustic emission characteristics and mechanical properties of 3d-printed stainless steel specimens including 420 (SS 420) series and 316L (SS 316L) series. Acoustic emission (AE), one kind of nondestructive testing (NDT), is widely applied in structure health monitoring and crack detection during dynamic processes. Using AE method, it is possible to detect fracture events of a specimen during the whole process of mechanical testing.

Results of AE analysis accompanying tensile tests present similar AE properties but no distinct differences between the two series. In AE figures, there are notable characteristics which indicate yield point and break point for samples with high ductility, while the notable characteristics can only indicate break point for specimens with low ductility. Also, the cumulative AE hits tend to decrease with increasing porosity of samples. Mechanical properties of SS 420 and SS 316 specimens are far away from those of standard materials, which may be caused by low packing density during printing or insufficient sintering.

TABLE OF CONTENTS

LIST OF TABLES

LIST OF FIGURES

ACKNOWLEDGMENT

First and foremost, I would like to express my sincere gratitude to my advisor, Dr. Qing-ming Wang, for his patient, enthusiasm, and instructive suggestions through my research. I could not have imagined how I could accomplish this thesis without his help and guidance.

I am also grateful to the rest of my thesis committee members: Dr. C. Garcia and Dr. Ian Nettleship, for their time and insightful comments.

I place on record my sincere gratitude to Yu Zhou, Sin Chien Siw, Bing Ma, Yu Gong, for their valuable experience and generous help with my experimental devices. My thanks also goes to Cong Huang, for his assistance in most of my experiments. My experiments would never be completed without their significant help.

I would like to thank my group members, Hongfei Zu, Huiyan Wu, Qiuyan, Rongjie Liang, Xuande Zhang, for their specialized knowledge and generous help.

I take opportunity to express my thanks to all the people who offered me help and support.

Last but not the least, I would like to thank my parents for unceasing support and encouragement and attention!

1.0 INTRODUCTION

1.1 BACKGROUND

Additive manufacture, also known as 3D printing, is a promising method to produce components with complicate geometry structure with less time and less cost than traditional manufacture methods. Acoustic emission is a widely used non-destructive testing method. There are many researches on either of them, but there is hardly a research combining both of them, so this research focus on evaluation of products by additive manufacture using acoustic emission.

1.2 OBJECTIVES OF THE RESEARCH

This research aims at establishing relationship between acoustic emission characteristics and mechanical properties of 3d-printed stainless steel specimens including 420 (SS 420) series and 316L (SS 316L) series. On the other hand, characterize porosity effect on mechanical properties.

2.0 LITERATURE REVIEW

2.1 OVERVIEW OF ACOUSTIC EMISSION (AE)

Acoustic Emission (AE) is a phenomenon of sound and ultrasound emitted as elastic waves in materials undergo deformation and fracture processes, for examples, moving dislocations and cracks. The real beginning of acoustic emission technology as we know it today was inaugurated in the 1950's [1], since then, there were extensive researches on AE theories and applications. Now acoustic emission has been broadly applied into three major areas: (1) structural testing and surveillance, (2) process monitoring and control, (3) materials characterization and testing.

2.1.1 Purpose of AE Research and Development

At first, it was pure interest of scientists to study acoustic emission phenomena. Then, with the increasing demand of heavy industries, like construction, aerospace and petroleum industry, for safety evaluation and structural health monitoring, the acoustic emission technique (AET) developed rapidly and many achievements were made not only on theory but also on application.

AET is unique among other non-destructive testing (NDT) methods with its own advantages. Compared to others, AET can survey long-term changes in materials behavior, especially the damage processes in materials being tested during the whole load history, and

without moving its components (for instance, sensors). These advantages lead to its unique ability to detect the presence of crack propagations both on the surface and deep inside a material. Ultrasonic analysis techniques, for example, have to be employed in combination with scanning techniques to observe a defect and require ceasing the loading. By contrast, only a few sensors being able to be fixed to the surface of the specimen are requested to monitor a structure or detect flaws under favorable conditions in AE studies. Moreover, there is no need to move the sensors for point-by-point scanning of the entire structure. All through-transmission methods demand access to both sides of the sample, but AET does not.

2.1.2 AE Signal Parameters

To analyze AE activity, the first step is discrimination AE signals from running waves because of rapid and random emergence of AE signals. Only the signals exceeding voltage threshold are recognized as AE signals. Definitions [2] of the prevailing signals are as follows.

1) Amplitude/ Signal peak amplitude: "The peak voltage of the largest excursion attained by the signal waveform from an emission event" (ASTM E1316-13d). This significant parameter determines the detectability of AE system. Amplitudes are expressed in decibels (dB) and 0 dB is defined as 1μv at sensor. The conversion equation is:

$$\text{Signal peak amplitude} = 20 \log10 (V_1/V_0)$$

where V_0 is reference voltage, typically 1μv at sensor and V1 is peak voltage of the measured acoustic emission signal.

2) Hit: "The detection and measurement of an AE signal on a channel" (ASTM E1316-13d). In Figure 2.1 [3], one hit matches one waveform.

3) Count: “the number of times the acoustic emission signal exceeds a preset threshold during any selected portion of a test” (ASTM E1316-13d). In Figure 2.1, one hit containing nine counts is observed. We notice that the employed threshold and the operating frequency have a strong influence on counts.

4) Duration: “the time between AE signal start and AE signal end” (ASTM E1316-13d). Generally, the duration is displayed on microseconds, which relies on source magnitude and noise filtering.

5) Rise time: “the time between AE signal start and the peak amplitude of that AE signal” (ASTM E1316-13d). The rise time has a close relation with the source-time function, and it is useful in the classification of fracture types or the elimination of noise signals.

6) Energy: “the total elastic energy released by an emission event” (ASTM E1316-13d). It indicates the magnitude of the source event.

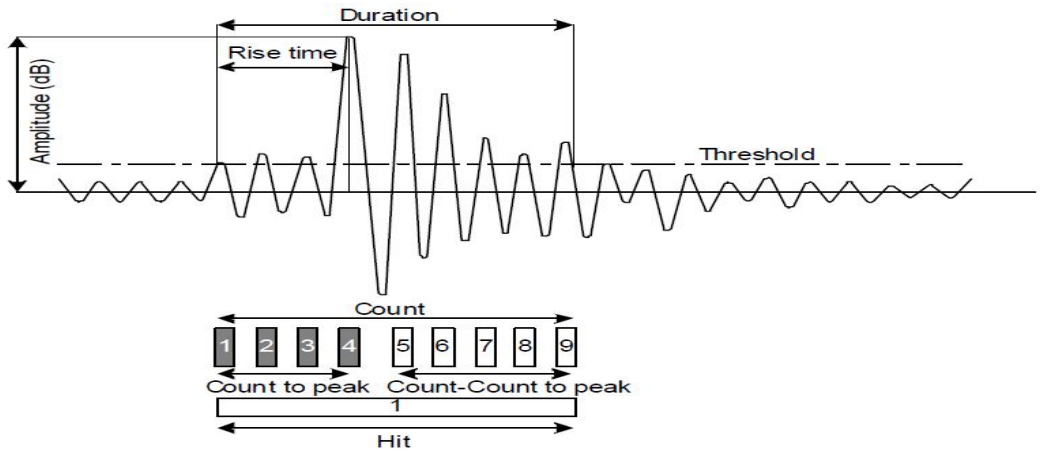

Figure 2.1 AE signal features [3]

2.1.3 AE Sources Mechanism

2.1.3.1 Two Types of AE Signals

AE signals generated by localized, rapid energy releases can be categorized as transient (burst type) signals and continuous signals. Most of events are transient ones, such as fast fracture and abrupt noise, which determines that the majority of AE signals are burst type. This type of AE signals is characterized as the clear start and end and obvious discrimination from background noise. Even those appearing continuous signals are mostly the superposition of large numbers of overlapping transient events [4]. Figure 2.2 demonstrates typical transient and continuous AE signals. Transient AE signals easily distinguished, but continuous AE signals resulting from leaks, flow and friction are barely discriminated from background noise because this type of AE signals and background noise are both broad band. Moreover the AE waveforms during dead-time for continuous signals are ignored by conventional AE record system. But Ito and Enoki [5] developed a AE measurement and analysis system named "Continuous Wave Memory" (CWM) to solve this problem.

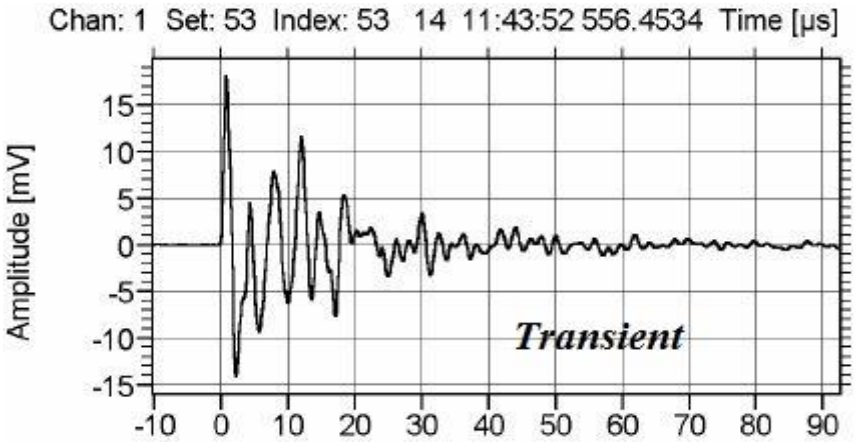

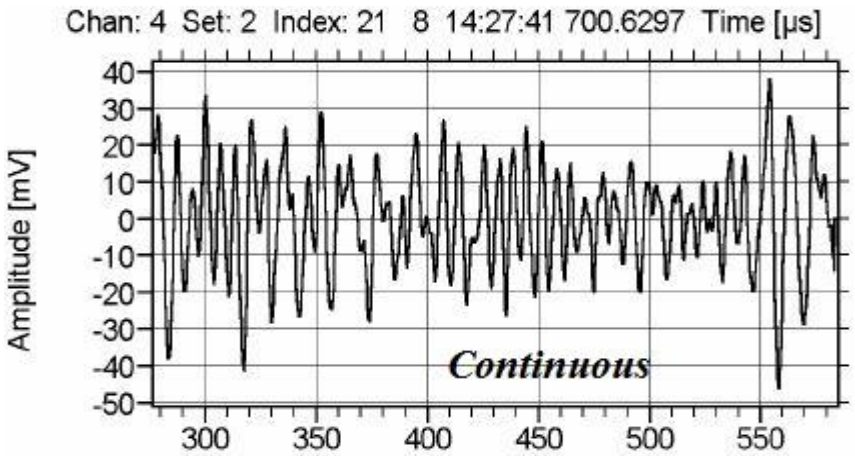

Figure 2.2 Typical transient and continuous AE signals [6]

2.1.3.2 Growing Crack AE Sources

A growing crack is one of the most significant and most researched AE sources. Once a crack is produced, its dimensions abruptly ramp up from zero. Simultaneously, local changes in stress and strain occur, which radiates elastic ultrasonic waves (AE).

Two basic types of cracks, brittle and ductile ones, are close related to the elastic waves (AE) radiated. For brittle fracture (Figure 2.3(a)), the stress change accompanied with a crack is large and swift, which generates high amplitude elastic waves conveying so large portion of the energy from sources that there is no enough energy for a crack to maintain the stable status and thus the crack propagates rapidly. For ductile fracture (Figure 2.3(b)), it grows slowly because in its enlarging plastic zone dislocations are driven by the majority of the energy from sources, which makes the tip of crack blunted fast. On this condition, the radiation as elastic waves can obtain much less energy from the crack. Scruby's research [7] demonstrated that the amplitude of AE signals are controlled by the rate of energy release, rather than the energy. This explains why brittle crack growth (Figure 2.3(a)) is readily detected and why ductile crack growth (Figure 2.3(b)) may be difficult to detect.

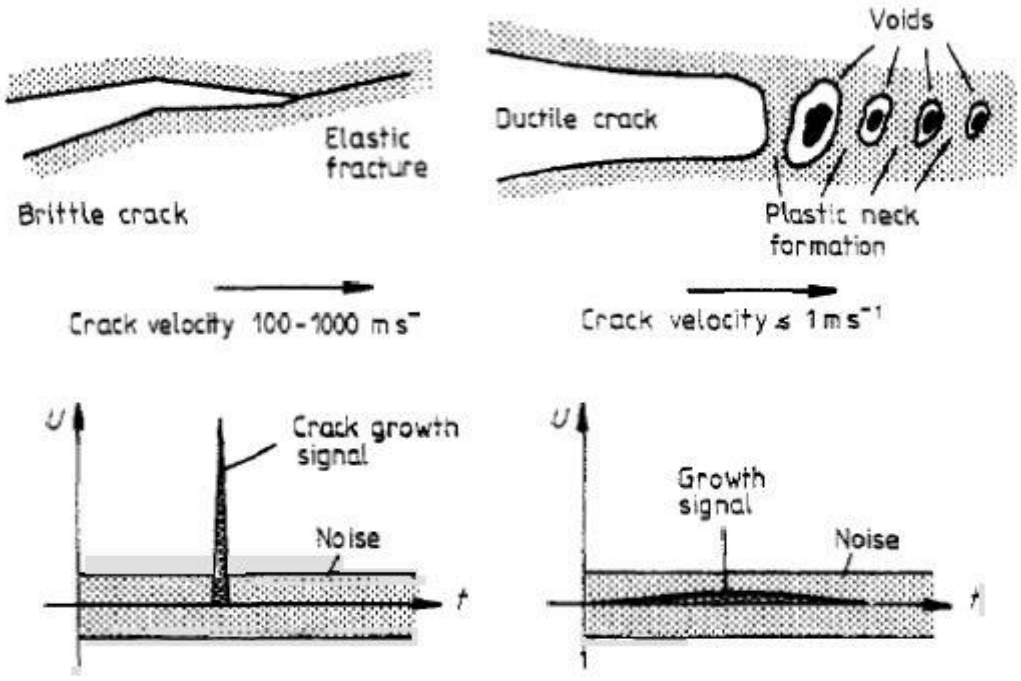

(a) (b)

Figure 2.3 Showing how (a) fast brittle crack advance generates detectable remission signals, while (b) slow ductile loading may not be detectable. [4]

2.1.4 Kaiser Effect and Felicity Effect

The Kaiser effect describes the phenomenon that acoustic emission occurs only after the previous maximum load is exceeded when material undergoes repetitive loading patterns. The Figure 2.4 is an example of the Kaiser effect .It was first investigated by Joseph Kaiser, who was considered as the father of modern AE technology because this research work of his in 1950 was the genesis of today's technology of acoustic emission. In the beginning, the Kaiser effect was called the irreversibility phenomenon by Kaiser himself. He stated in the English translation of his dissertation [8]: "As is known, plastic strain, however slight, is irreversible. This suggests that the acoustic effects obtained in our experiments also involve irreversible processes."

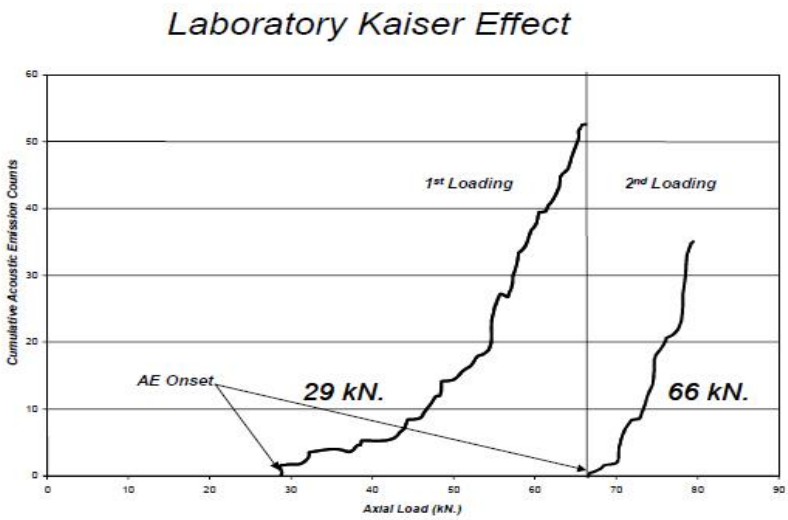

Figure 2.4 An example of Kaiser Effect. [9]

The Felicity effect is a breakdown of the Kaiser effect, which means that emission occurs before the preceding maximum load is surpassed when material undergoes repetitive loading patterns. Dr. Fowler discovered this phenomenon in composite materials [10] and named it after his daughter Felicity. The quantification of the Felicity is achieved by the Felicity ratio.

$$\text{Felicity Ratio} = \frac{\text{the load where AE resumes}}{\text{the preceding maximum load}}$$

Besides this, invalidity of the Kaiser effect also results from time dependent processes like stress corrosion and hydrogen embrittlement

2.2 PREVAILING DESIGN OF TODAY'S AE SYSTEM

As is shown in Figure 2.5, the AE system today typically consists of a sensor, preamplifier, filter, and main amplifier as well as measurement, storage, and display equipment. The system can be single-channel or multichannel.

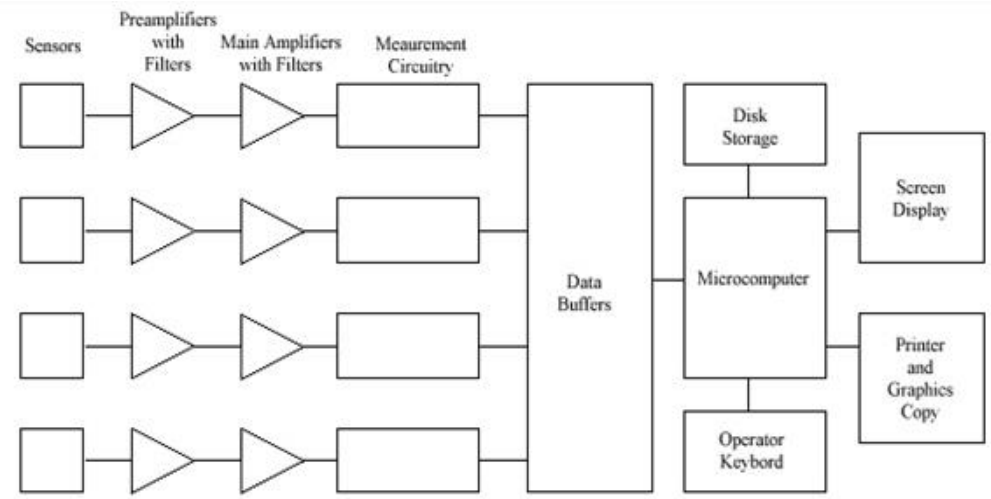

Figure 2.5 Schematic Diagram of a Basic Four-channel Acoustic Emission Testing System [11].

AE Sensor

The first part of AE system is the sensor which is significant. Only signals that AE sensor obtained can be processed by the subsequent measurement system, and others will be lost for analysis. These effective signals are transformed by the AE sensor from the surface movement caused by an elastic wave. Usually, AE sensors are directly attached to the surface of the object (Figure 2.6).

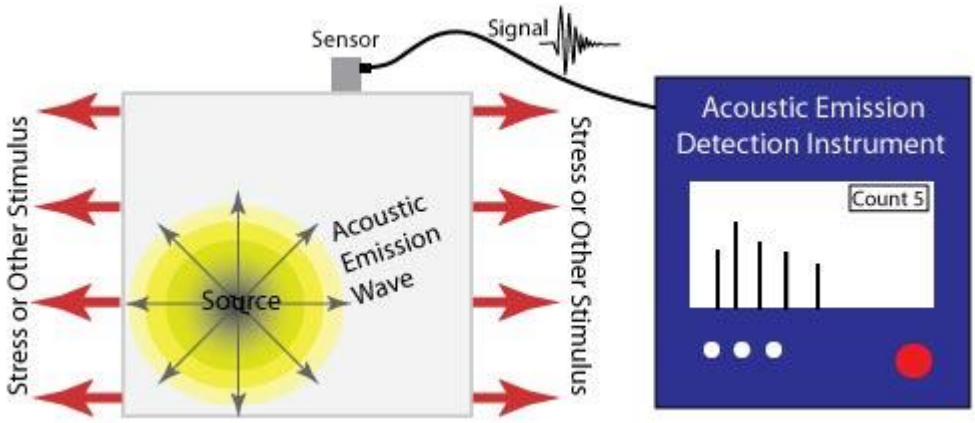

Figure 2.6 Detection of AE wave. [12]

The core part of the AE sensor consists of the piezoelectric element with high sensitivity which can convert surface movement to an electrical voltage efficiently. In the most situations,

a piezoelectric element in a protective case with damping material inside as illustrated in Figure 2.7 is applied to detection. Thus the sensors are merely grounded on the piezoelectric effect out of lead zirconate titanate (PZT).

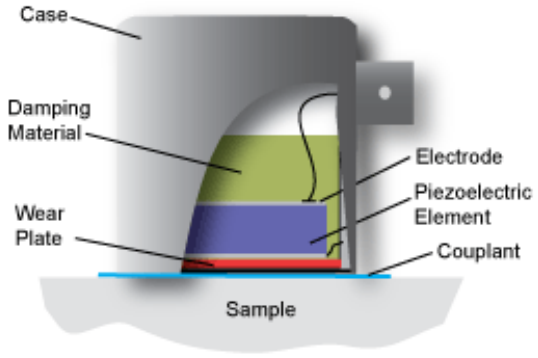

Figure 2.7 AE sensor with the piezoelectric element. [11]

Choosing an appropriate sensor for a specific AE application is the key to success of the measurement. The main criterion for the AE-sensor selection is the frequency response which must fit the application. For majority of applications, there are three widely used frequency regimes: low (20 kHz - 100 kHz), standard (100 kHz - 400 kHz) and high (>400 kHz). Frequencies above 400 kHz are usually meaningless and are cut-off for minimizing electronic noise, since attenuation per unit distance rises with increasing frequency.

AE sensors are broadly classified into two types: resonance models and wide band width models. For resonant AE sensors, they have a narrow bandwidth and are highly sensitive exclusively at their resonance frequency, which are often employed if the aim is not the frequency content itself but only AE features like amplitude, energy or arrival time. It is comparable for those AE features only when they are recorded with the identical AE sensor type, because AE features are influenced by the peak frequency and frequency range of the AE sensor. The resonance frequency is the decisive factor for selecting resonant AE sensors. For

wideband AE sensors, they possess uniform sensitivity across a broad band of exciting frequencies. Wideband AE sensors with a flat response curve are generally demanded on the condition of unknown frequency of interest or analysis of different frequencies in one signal.

Determining the proper frequency range for a specific application must consider factors such as material, specimen size and background noise. In lower frequency range (<100 kHz) background noise is normally more dominant. In higher frequency range, false triggering can be avoided.

Certain frequency ranges have been proven to be best suitable for specific applications.

Table 2.1 AE Frequency for Application

Application	20-100 kHz	100-400 kHz	>400 kHz
Corrosion screening of flat bottom storage tanks	X		
Leakage detection in water/oil pipelines	X		
Hot reheat pipe crack detection		X	
Integrity testing of pressure vessels		X	
Partial discharge detection	X (when noise is low)	X	
Integrity testing of metallic structures		X	
Integrity testing of composite materials		X	
Integrity testing of concrete structures	X		
Drying process monitoring of plants/wood		X	
AE-testing of small specimen			X

2.3 AE SOURCE LOCALIZATION

2.3.1 One-Dimensional Localization

For an object whose dimension in one axis is much larger than the ones in the other two axes, we can consider the object one-dimensional. Two sensors are enough to localize fracture by the following method which is named linear localization method.

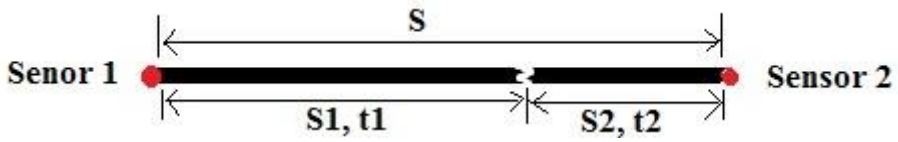

Figure 2.8 Linear Localization

From Figure 2.8, we can derive these equations to determine the source location.

$$v*(t_1-t_0) = S_1$$

$$v*(t_2-t_0) = S_2$$

$$S_1+S_2 = S$$

V is the velocity of sound in the object, S is the distance between two sensors, S_1 and S_2 are the distances from fracture source to each sensor, t_0 is the source time, and t_1 and t_2 are onset time at each sensor. As S, t_1 and t_2 are easily measurable and v is known, we can determine t_0 by solving the three equations.

In practice, the AE source is often uncertain so that three or more sensors identical spaced are needed to define the location area of the source, which is known as zone localization method. By recognizing the first and the second hit AE sensors (transducers), we can identify the source area. As is shown in Figure 2.9, transducer 3 receives the first hit and transducer 2 receives the second hit, so the source exists between transducer 2 and 3 but it is closer to transducer 3. Following zone localization, linear localization is utilized to locate the source.

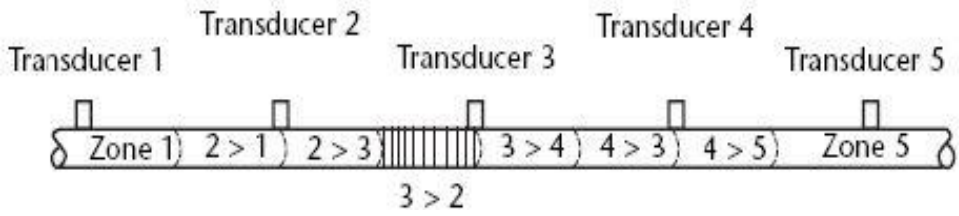

Figure 2.9 Schematic of zone localization [13]

2.3.2 Two-Dimensional Localization

On planar condition, a triangular sensor array is applied to determine the source location in two-dimension. See Figure 10, the AE source is at the intersection of two-hyperbolae. Three sensors S_1, S_2 and S_3 are placed at positions (x_1, y_1), (x_2, y_2) and (x_3, y_3). (x_s, y_s) is the source location needed to be determined. D_1, D_2 and D_3 are distances between sensors. Source-sensor distances include d_1, d_2 and d_3. Time that elastic waves travelling from source to each sensor is t_1, t_2 and t_3. Arrival time difference between S_2 and S_1 is $\Delta t_1 = t_2 - t_1$ and that between S_3 and S_1 is $\Delta t_2 = t_3 - t_1$. AE wave velocity is c.

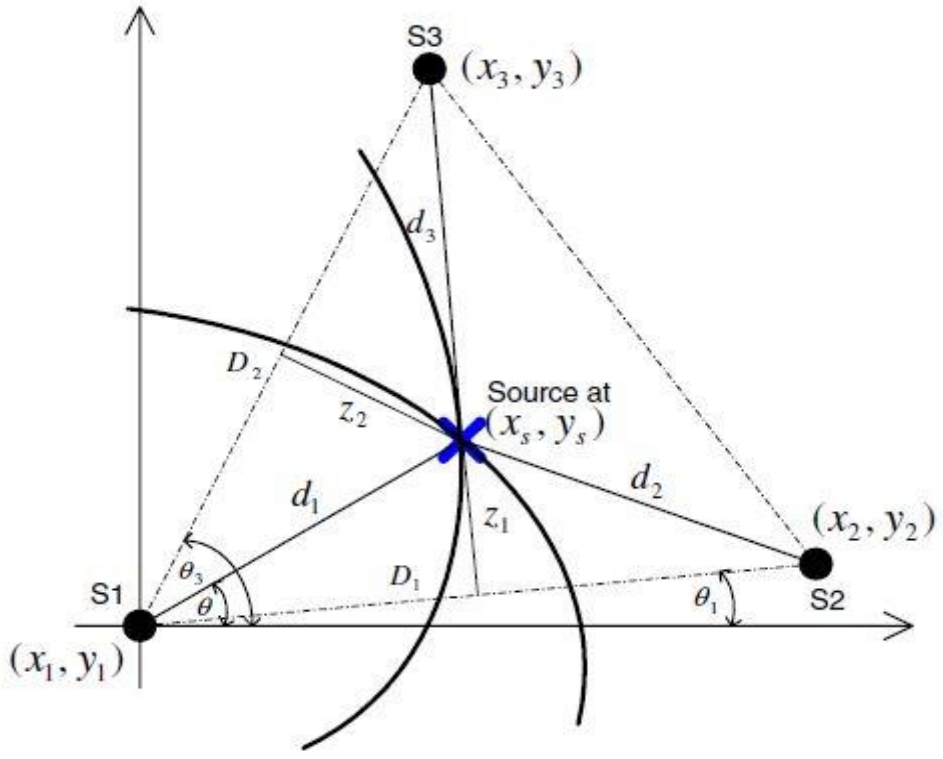

Figure 2.10 Schematic diagram of two-dimensional localization. [14]

The distance between sensor S1 and the source can be expressed by [14] :

$$d_1 = \frac{D_1^2 - \delta_1^2}{2(\delta_1 + D_1 \cdot \cos(\theta - \theta_1))}$$

$$d_1 = \frac{D_2^2 - \delta_2^2}{2(\delta_2 + D_2 \cdot \cos(\theta_3 - \theta))}$$

where angles θ,θ_1 and θ_3 are defined in Figure 2.10 and

$$\delta_2 = d_2\text{-}d_1 = c(t_2\text{-}t_1) = \Delta t_1 \cdot c$$

$$\delta_1 = d_3\text{-}d_1 = c(t_3\text{-}t_1) = \Delta t_2 \cdot c$$

Above these equations, D1, D2, θ_1, θ_3 are what we already known, and c, Δt_1 and Δt_2 can be measured by AE system. Combining the equations, d_i (i = 1, 2, 3) and θ are all solved. Thus, the source location can be calculated by

$$x_s = x_1 + d_1 \cdot \cos\theta,$$

$$y_s = y_1 + d_1 \cdot \sin\theta.$$

2.3.3 Three-Dimensional Localization

The 3-D localization problem needs at least four available travel times to determine the source location so that at least four AE sensors are demanded. If the AE source resembles a point source in a homogenous and isotropic material, the iterative localization method can give a solution.

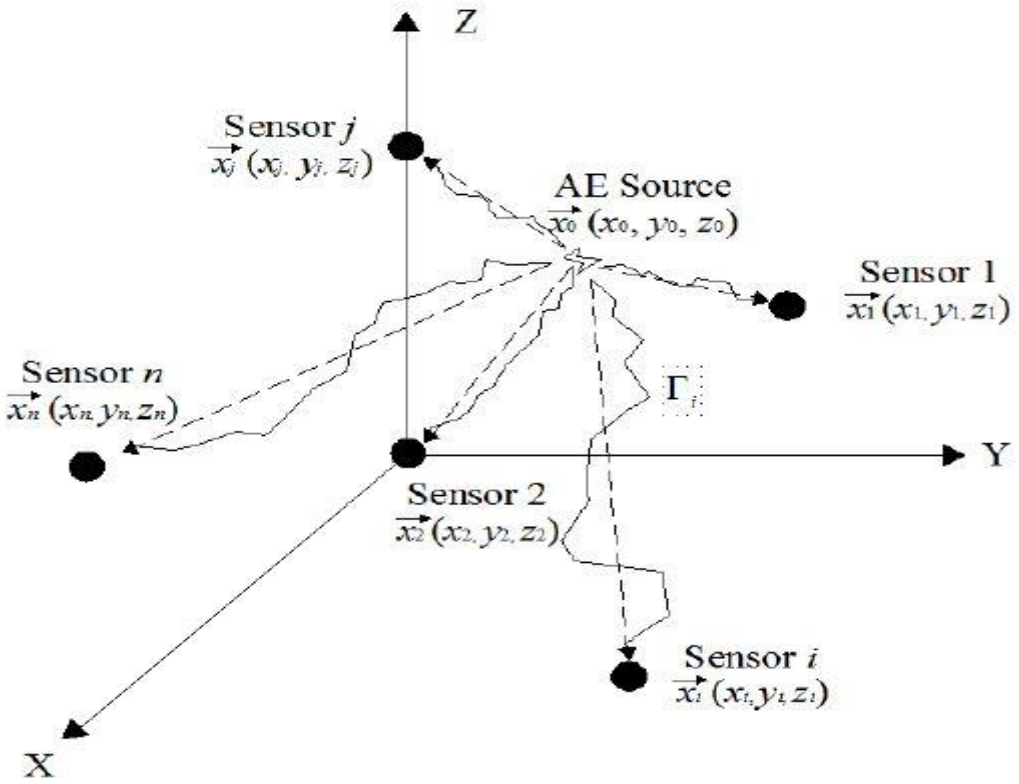

Figure 2.11 Localization of point AE source involving a generic array of n sensors. [15]

From Figure 11, the onset time t_i^* at sensor $\vec{x_i}$ can be given by:

$$t_i^* = t_0 + |\vec{x_i} - \vec{x_0}| / v_p = t_0 + \vec{x_{i0}} / v_p, \text{ [15]}$$

where $\vec{x_0}$ is unknown crack coordinate, t_0 is origin time and v_p is wave velocity. Between the detected onset time t_i and the calculated onset time t_i^*, there exists residual r_i for each sensor i:

$$r_i = ti - t_i^* \text{ . [15]}$$

$\vec{r}$ is the data vector with the residuals for n observations of one AE event. Applying corrections $\Delta\vec{x}$ and Δv_p to the source parameters, we have:

$$A^T A\vec{r} = -A(\Delta\vec{x}, \Delta v_p)^T \text{ . [15]}$$

A, a (n-1)×4 matrix, calculated at $\vec{x_0}$ can be expressed by:

$$\mathrm{A} = \begin{bmatrix} \frac{\partial r_2^*}{\partial x} & \frac{\partial r_2^*}{\partial y} & \frac{\partial r_2^*}{\partial z} & \frac{\partial r_2^*}{\partial v_p} \\ \vdots & \vdots & \vdots & \vdots \\ \frac{\partial r_n^*}{\partial x} & \frac{\partial r_n^*}{\partial y} & \frac{\partial r_n^*}{\partial z} & \frac{\partial r_n^*}{\partial v_p} \end{bmatrix} . [15]$$

We can iteratively solve the problem until convergence by utilizing the linearization of the equation $A^T A\vec{r} = -A(\Delta\vec{x}, \Delta v_p)^T$, beginning with a first guess for the AE source location. The initial guess should lie close to the true source location. Thus, the geometry center of the specimen is a feasible choice for smaller samples and the first-hit sensor can be selected for lager samples.

2.4 AE BEHAVIORS DURING DEFORMATION

According to ductility and malleability, materials can be classified into two types: one is ductile material, and the other is brittle material. Ductile materials experience observable plastic deformation prior to fracture. Brittle materials experience little or no plastic deformation prior to fracture. AE signal generated during plastic deformation of a ductile material has been researched by numbers of scientists.

Deformation of materials can be represented by stress-strain diagrams. Figure 2.12 shows a typical ductile material, while Figure 2.13 demonstrates brittleness of a material.

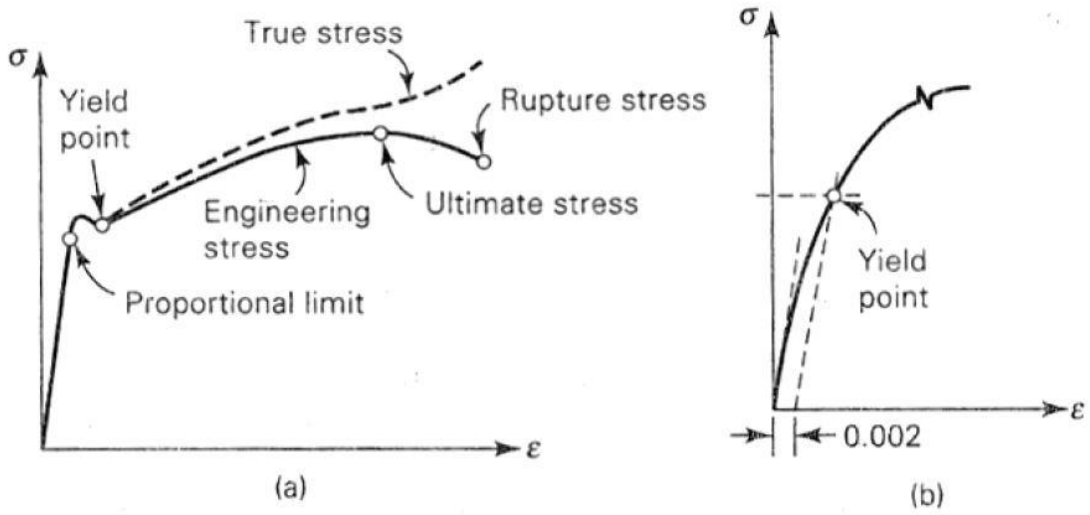

Figure 2.12 (a) Typical ductile material stress-strain curve;
(b) determination of offset yield strength [16]

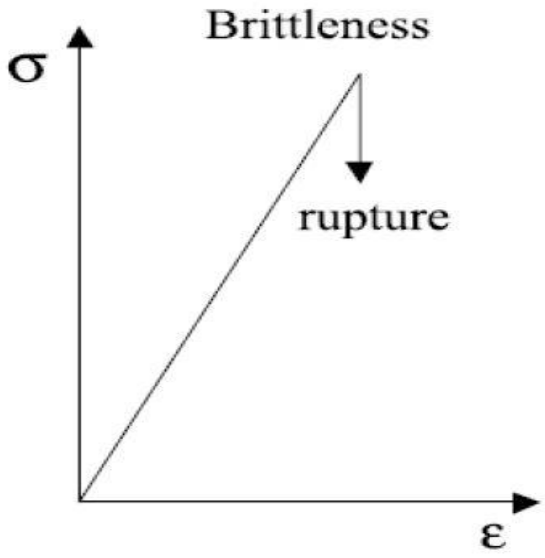

Figure 2.13 Brittleness as characterized by the stress-strain curve σ(ε). Brittleness is characterized by the absence of inelastic strain before failure. [17]

During the deformation under tensile stress, there occurs maximum AE activity close to the yield region [18]. The amplitude distribution of AE sources are usually expressed by a histogram of the distribution of maxima of AE sources (Figure 2.14). As shown in Figure 2.15, Han et al. [19] divided the tensile process into four distinct regimes: (1) the micro-plastic deformation stage, (2) the yielding stage, (3) the strain hardening stage and (4) the necking and

fracture stage, with the first stages generating significant AE signals. In stage 3 the AE energy and events gradually decreased after macro-yielding. Plenty of AE signals were received when the final fracture happened. Similar results were obtained by other studies [20, 21] for metal materials.

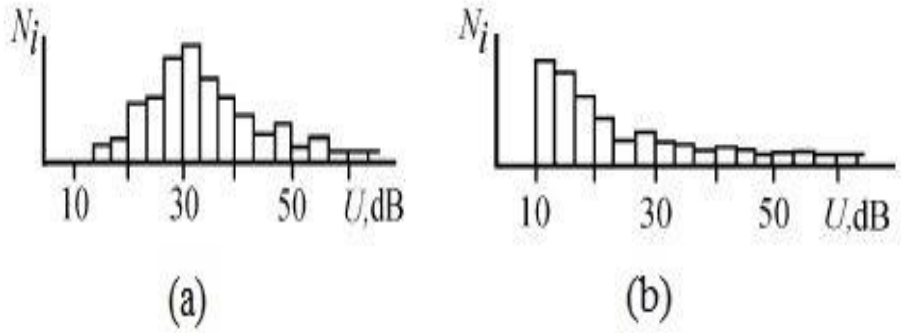

Figure 2.14 Amplitude distribution of AE signals during brittle (a) and ductile (b) fracture of materials [22]

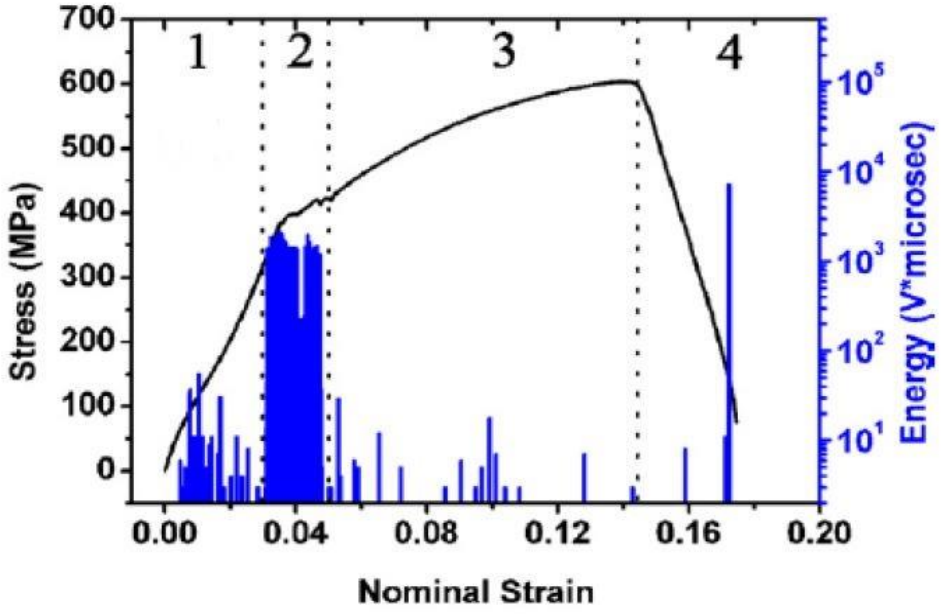

Figure 2.15 Stress and AE energy versus nominal strain [19]

2.5 MECHANICAL TEST

2.5.1 Tensile Test

Tensile test is also called tension test. The engineering tension test is widely used to provide basic design information on the strength of materials and as acceptance test for the specification of materials [23]. In tensile test, a specimen is subjected to an increasing controlled tension until fracture. In this research, we operated the most commonly used one – uniaxial tensile test. During the process, elongation of the specimen is observed along with the increase of tension. Ultimate tensile strength, elongation after fracture and reduction of area can be directly measured. Derived from these measurements, we can determine other properties such as yield strength, Young's modulus and Poisson's ratio.

The apparatus of tensile testing consists of testing machines, gripping devices, dimension-measuring devices and extensometers. As shown in Figure 2.16, grips should be chosen in accordance with geometry of the test specimen. In this thesis, our test specimens were sheet-type so that serrated wedges were chosen and the scale of specimens were determined based on the standard of ASTM (Figure 2.17).

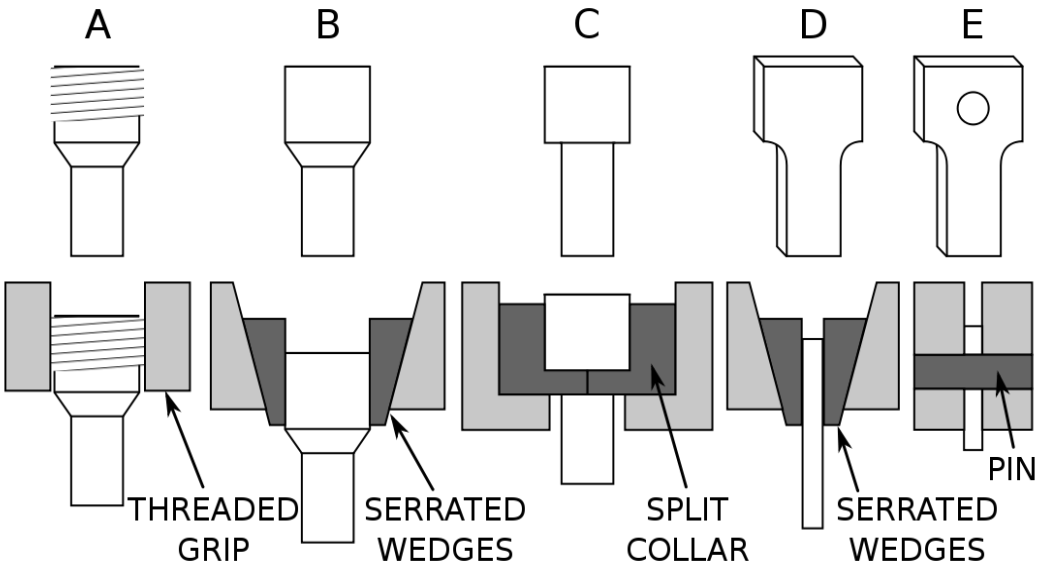

Figure 2.16 Various shoulder styles for tensile specimens. Keys A through C are for round specimens, whereas keys D and E are for flat specimens. [24]

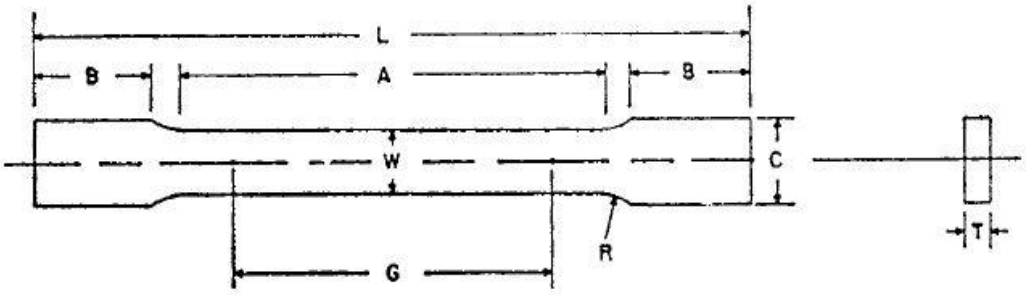

	Dimensions		
	Standard Specimens		Subsize Specimen
	Plate-Type, 40 mm [1.500 in.] Wide	Sheet-Type, 12.5 mm [0.500 in.] Wide	6 mm [0.250 in.] Wide
	mm [in.]	mm [in.]	mm [in.]
G—Gauge length	200.0 ± 0.2 [8.00 ± 0.01]	50.0 ± 0.1 [2.000 ± 0.005]	25.0 ± 0.1 [1.000 ± 0.003]
W—Width	40.0 ± 2.0 [1.500 ± 0.125, -0.250]	12.5 ± 0.2 [0.500 ± 0.010]	6.0 ± 0.1 [0.250 ± 0.005]
T—Thickness (Note)		thickness of material	
R—Radius of fillet, min	25 [1]	12.5 [0.500]	6 [0.250]
L—Overall length, min	450 [18]	200 [8]	100 [4]
A—Length of reduced section, min	225 [9]	57 [2.25]	32 [1.25]
B—Length of grip section, min	75 [3]	50 [2]	30 [1.25]
C—Width of grip section, approximate	50 [2]	20 [0.750]	10 [0.375]

NOTE—The dimension T is the thickness of the test specimen as provided for in the applicable material specifications. Minimum thickness of 40 mm (1.500 in.) wide specimens shall be 5 mm (0.188 in.). Maximum thickness of 12.5 and 6 mm (0.500 and 0.250 in.) wide specimens shall be 19 and 6 mm (0.750 and 0.250 in.), respectively.

Figure 2.17 Rectangular Tension Test Specimens. [25]

Typical stress-strain curve for a ductile material can be achieved from the tensile test data, as depicted in Figure 2.18. From the origin to point A, the Hooke's Law is obeyed and stress is directly proportional to strain. Thus, the point A is called proportional limit. The straight line zone is elastic region, in which a material can restore its origin shape after the load is removed. Young's modulus can be obtained by the slop of this straight line. The point B is known as 0.2% offset yield strength or proof stress which is usually regarded as yield strength in engineering fields. The point B is determined by the intersection of stress-strain curve and a straight line which is parallel to line OA and whose X intercept is 0.2% strain. Beyond the point A, inelastic deformation begins to take place; from the point B, deformation is totally plastic. The zone between the point A and the point B is known as yield region and is featured as the drop of stress. This phenomenon is related to dislocation motion. Before it happens, mobile dislocations are too few to cause slip until sufficient stress is applied to a source to cause dislocation multiplication [26]. Then the produced dislocations are able to glide rapidly across grains, resulting in the abrupt reduce of stress. The stress increases with increasing strain up to the point C at which the maximum stress is reached during the whole tensile test. So the point C is termed as ultimate tensile strength (UTS). This region is named after strain hardening which works in this region. Because of generation of large numbers of dislocations, their density are high enough to make their interaction possible to impede movement, leading to an increase in yield strength but a decrease in ductility. Beyond the point C, a material's cross-section decreases greatly faster than that in strain hardening region, which gives rise to necking in this material. As a result, the last region is named as necking region. At the point D, the specimen finally fractures.

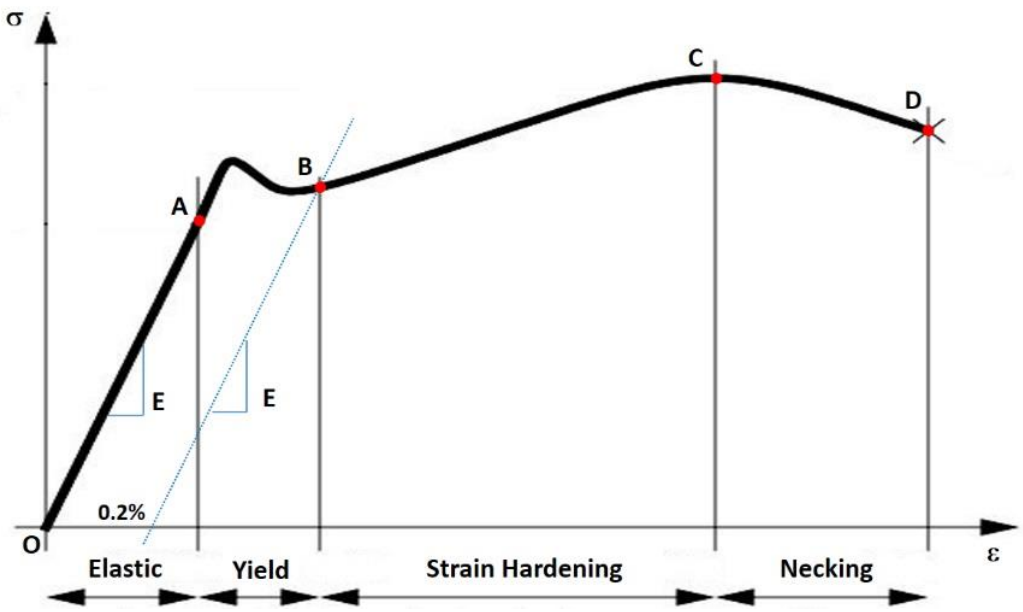

Figure 2.18 Stress-strain Curve

2.5.2 Hardness Testing

Hardness is a measure of resistance to deformation, including but not limited to elastic or plastic deformation, bending, scratching abrasion or cutting. For metals, hardness usually refers to resistance to permanent or plastic deformation. There are three general types of measurements: scratch hardness, indentation hardness and rebound hardness.

Scratch hardness is measured by Mohs' scale which was created by the German geologist and mineralogist Friedrich Mohs in 1812. The principle is that the one of two materials is harder if it can visibly scratch the other. According to this principle, 10 chosen minerals as criteria are scored from 1-10. Talc is the softest one with the value 1 while the diamond is the hardest with a hardness of 10. Most hard metals fall in the Mohs' hardness range of 4 to 8 [23]. Obviously, this method is convenient to conduct, especially in field, but it cannot accurately gauge the hardness of materials.

Indentation hardness is widely applied in Engineering and metallurgy fields to measure the resistance of a material to deformation. Rockwell, Brinell and Vickers are generally used indentation scale. In this research, Vickers hardness was employed, which was developed by Smith and Sandland at Vickers Ltd. in 1921 [27]. This test method uses a square-base right pyramid diamond with an angle of 136 degrees between opposite faces, as depicted in Figure 2.19. When using kgf and mm, Vickers hardness is determined as follow:

$\text{HV} = \frac{2P_1 \sin(136°/2)}{D_1^2} = 1.8544 \times P_1/D_1^2$ [28]

where: P_1 = force, kgf and

D_1 = mean diagonal length of the indentations, mm.

When units of GPa are in use, the Vickers hardness is calculated by the following formula:

$\text{HV} = 0.0018544 \times P_2/D_2^2$ [28]

where: P_2 = force, N, and

D_2 = mean diagonal length of the indentations, mm.

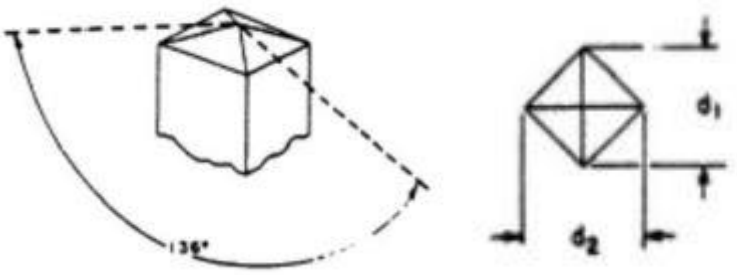

Figure 2.19 Vikers Indenter [28]

Rebound hardness implies the elasticity of a material, which is also known as dynamic hardness. A diamond-tipped hammer falls from a fixed height onto the material to be tested. The value of rebound hardness relies on the hammer rebound height: the higher the hammer reboundsmerize, the harder the material is.

2.6 ADDITIVE MANUFACTURE (AM)

Additive Manufacture is an advanced technology which build up 3D objects layer by layer. In additive manufacturing processes, the computer-aided design (CAD) software is used to design the 3D models of our desired component. Then the CAD file needs to be converted to a stereolithography (STL) file which is also called Standard Tessellation Language so that AM system can recognize. The STL file stores the information for every layer by dividing the model into slices.

Rapid prototyping is one of the most common applications of AM. As is shown in Figure 2.20, rapid prototyping saves large amount of time since there is no casting, no machining, and even no assembling in the processes.

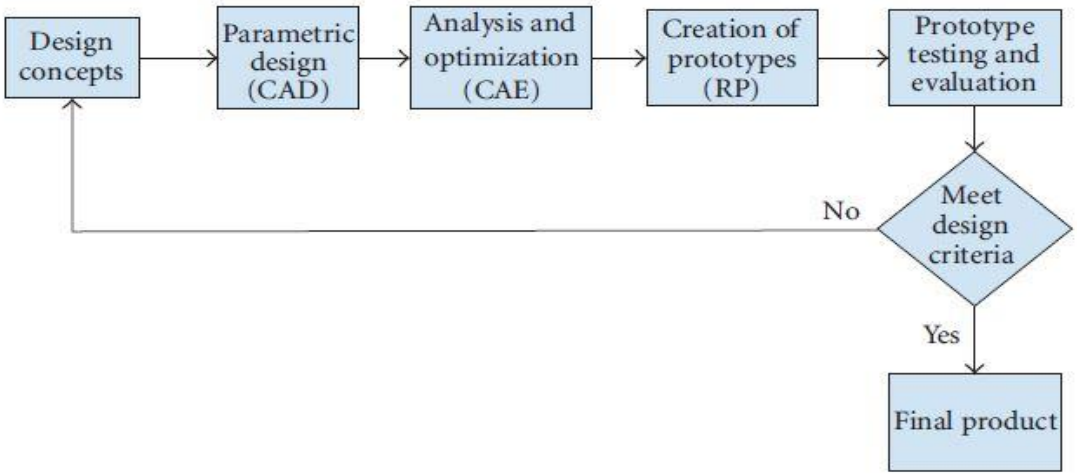

Figure 2.20 Product development cycle of using rapid prototyping [29]

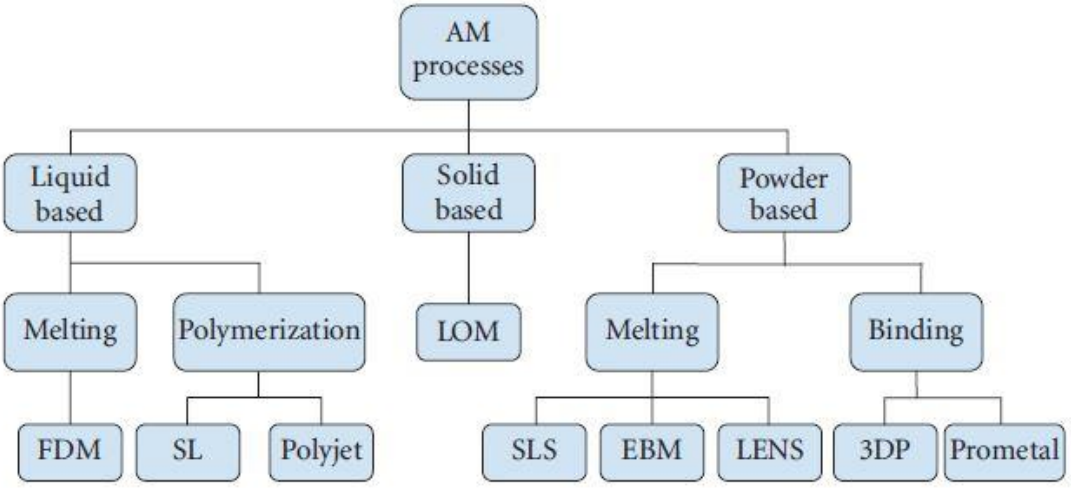

Figure 2.21 Classification of additive manufacture [30]

In Figure 2.21, there is an overview of the different additive manufacturing processes containing stereolithography (SL), Polyjet, fused deposition modeling (FDM), laminated object manufacturing (LOM), 3D printing (3DP), Prometal, selective laser sintering (SLS), laminated engineered net shaping (LENS), and electron beam melting (EBM) [30].

In this research, what we used is Prometal which is a powder-based AM process for metals. This method is based on three dimensional printing developed at MIT [31]. Figure 2.22 and Figure 2.23 demonstrate 3D printing and prometal printing process in general, respectively. The two printing methods are nearly the same in process except for some improvement added for prometal printing. In our printing process, the recoater unloads metal powder and paves it on a powder bed, then a feed piston supplies the recoater with metal power. Next, nozzles spurt out liquid binder in jets to metal powder. After the recoater heats and dries the powder, one layer is finished and the powder bed will be lowered for the next layer. When all the layers are finished, a model is accomplished. If a functional part is being built, sintering, infiltration, and finishing processes are required [32].

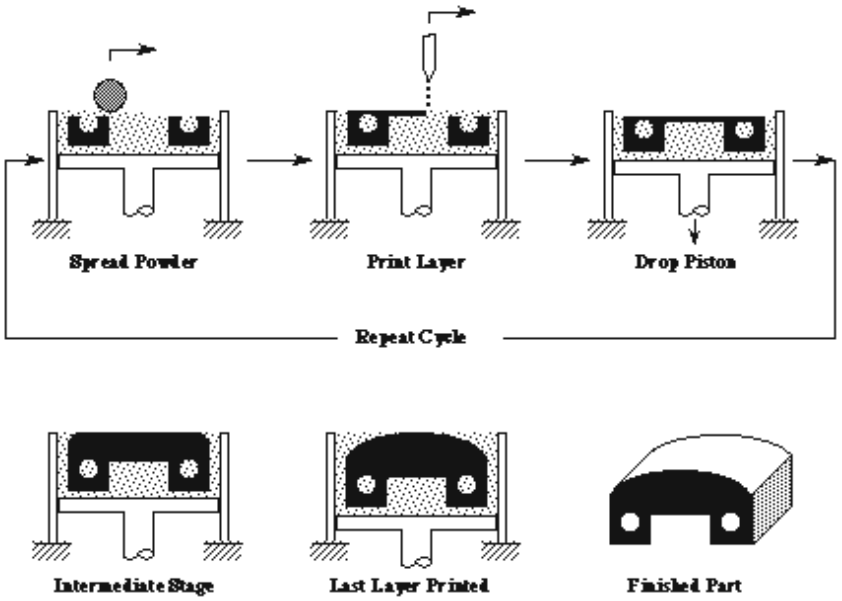

Figure 2.22 Three dimensional printing (3DP) process [31]

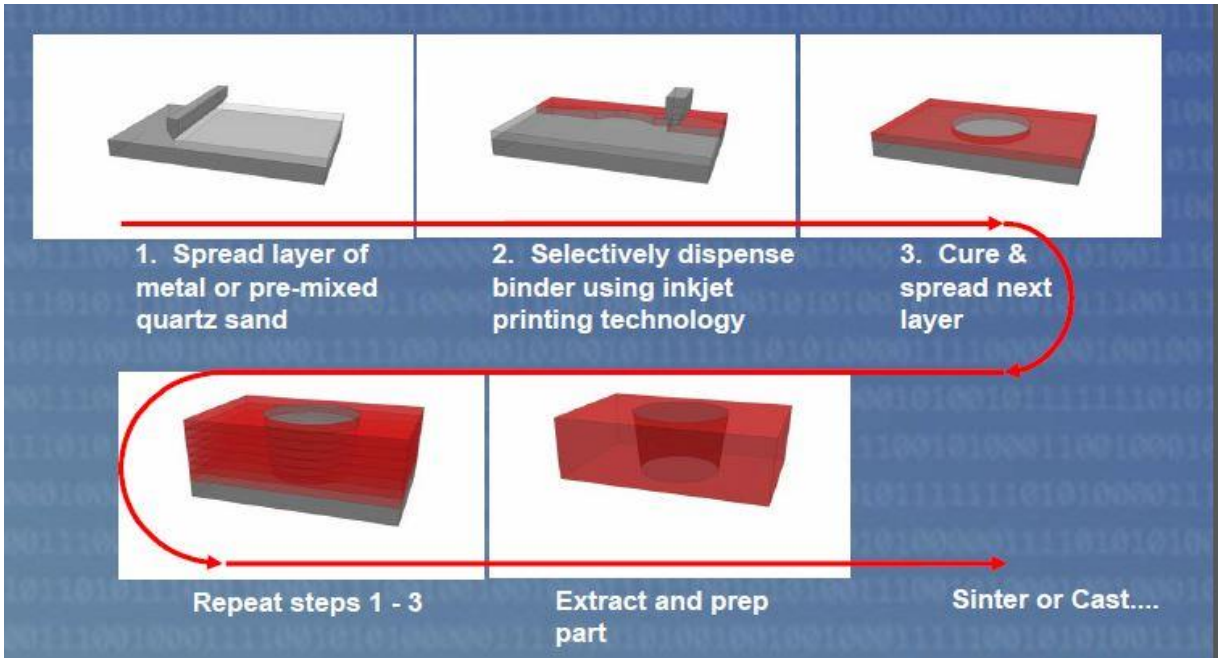

Figure 2.23 Prometal printing pocess [33]

3.0 EXPERIMENTAL PROCEDURES

3.1. ADDITIVE MANUFACTURE

Green parts were produced by 3D printer with 420 stainless steel powders and 316L stainless steel powders. Their compositions are shown in Table 3.1.

Table 3.1 Powder Composition (wt%)

Alloy	Fe	C	Cr	Ni	Mo	Si	Mn	S	P	N
SS 316L	Bal.	0.03	16.0-18	10.0-14.0	2.0-3.0	1	2	0.03	0.045	\
SS 420	Bal.	0.27	14.0	0.07	1	0.62	0.03	0.01	\	0.024

3.2. CURING

Once printing process was completed, the draw box containing printed products was immediately carried to the drying oven for debinding. Otherwise, residual binder would react and become chemical harmful to the products at high temperature during sintering. The drying temperature was set as 200 ℃ and the holding time was 4 hours.

3.3. SINTERING

Specimens are only pile-up of powder particles without grain inside right after curing. So it is essential to conduct sintering for crystallization. According to our previous study, higher sintering temperature and less holding time would result in products with better properties. Finally, the sintering temperature was determined at 1360 ℃ and 1375 ℃ and the holding time was determined as 90 minutes. Heating rate was 5 ℃/min and cooling rate was 3 ℃/min considering that higher rate would harm the tube used for sintering. The sintering profile is depicted in Figure 3.1.

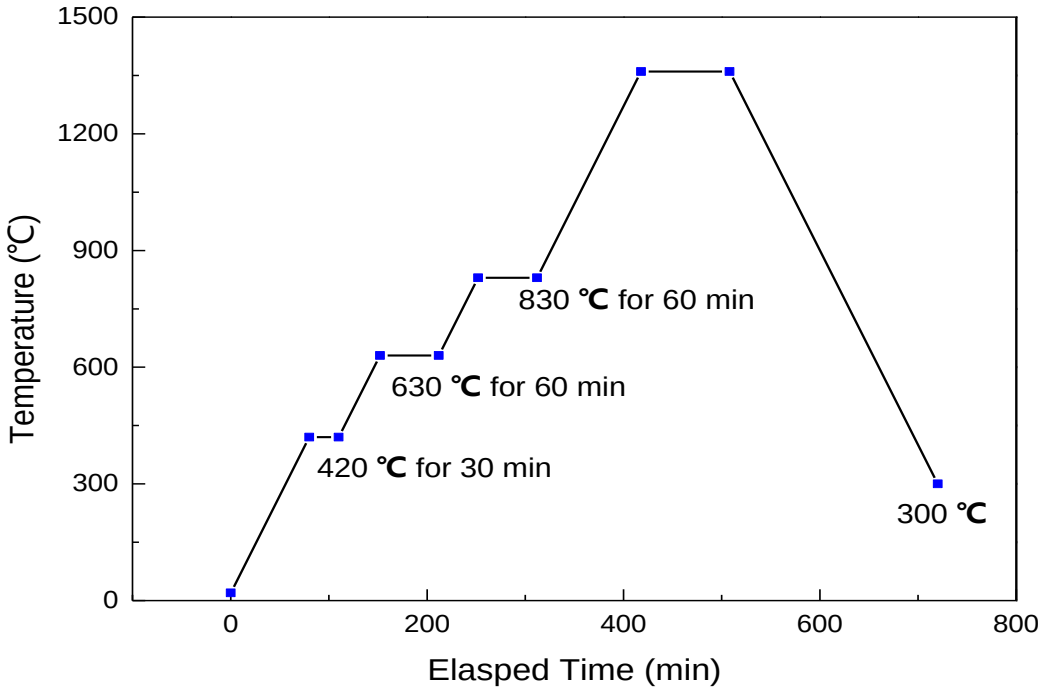

Figure 3.1 Sintering Profile

3.4. TENSILE TEST WITH AE

Tensile tests were conducted by MTS machine under monitor of AE system. Two AE sensors were mounted separately at two ends of specimen after sintering. The strain rate was 2 mm/min.

3.5. DENSITY MEASUREMENT

Buoyancy method is widely utilized to determine the density of specimens. Firstly, dry weight M_0 of the object is measured. Then cover the sample with a layer of grease as thin as possible and hang it on and make it totally immersed in liquid (usually water). At first, the total weight of container and liquid is M_1, while the total weight changes into M_2 after the object is immersed. The weight change indicates the magnitude of buoyancy. Thus the density of the object is calculated by the following expression:

$$\rho = \rho_{liquid} * M_0/(M_2-M_1)$$

where ρ_{liquid} is the density of liquid in the container.

Due to the size limit of the scale, every specimen was cut into three or four pieces.

3.6. VICKERS HARDNESS

For each specimen, 10 points were chosen to measure Vickers hardness, and their average value is the final result. Loading time was set as 10 seconds.

4.0 RESULTS AND DISCUSSIONS

4.1 TENSILE TESTS MONITORED BY AE

4.1.1 SS 316L Series

This series contains 6 specimens which are divided into two groups: one is sintered at 1360 ℃ with 90-min holding time and the other is sintered at 1375 ℃ with 90-min holding time. They are labeled as SS 316L-1360-1, SS 316L-1360-2, SS 316L-1360-3, SS 316L-1375-1, SS 316L-1375-2 and SS 316L-1375-3, respectively. In Figure 4.1(a)-(f), the blue curve is stress-strain curve during the tensile test, the green curve stands for hit rate from channel 1, and the red one represents hit rate from channel 2. According to the stress-strain curve, the whole process of this tensile test can be broadly classified into four regions from low strain to high strain, that is, (I) elastic region, (II) yield region, (III) plastic region and (IV) necking and fracture region. Since there is no distinct yield phenomenon shown in any curve, the yield region is set as the zone between proportionality limit point and offset yield strength point. Figure 4.1(a)-(f) show the same tendency of hit rate change: as the strain increases, AE hit rate rises at region I and II, then it decreases after the first noticeable peak and fluctuates at lower level at region III, and finally it suddenly increases dramatically at region IV, which forms the last noticeable peak.

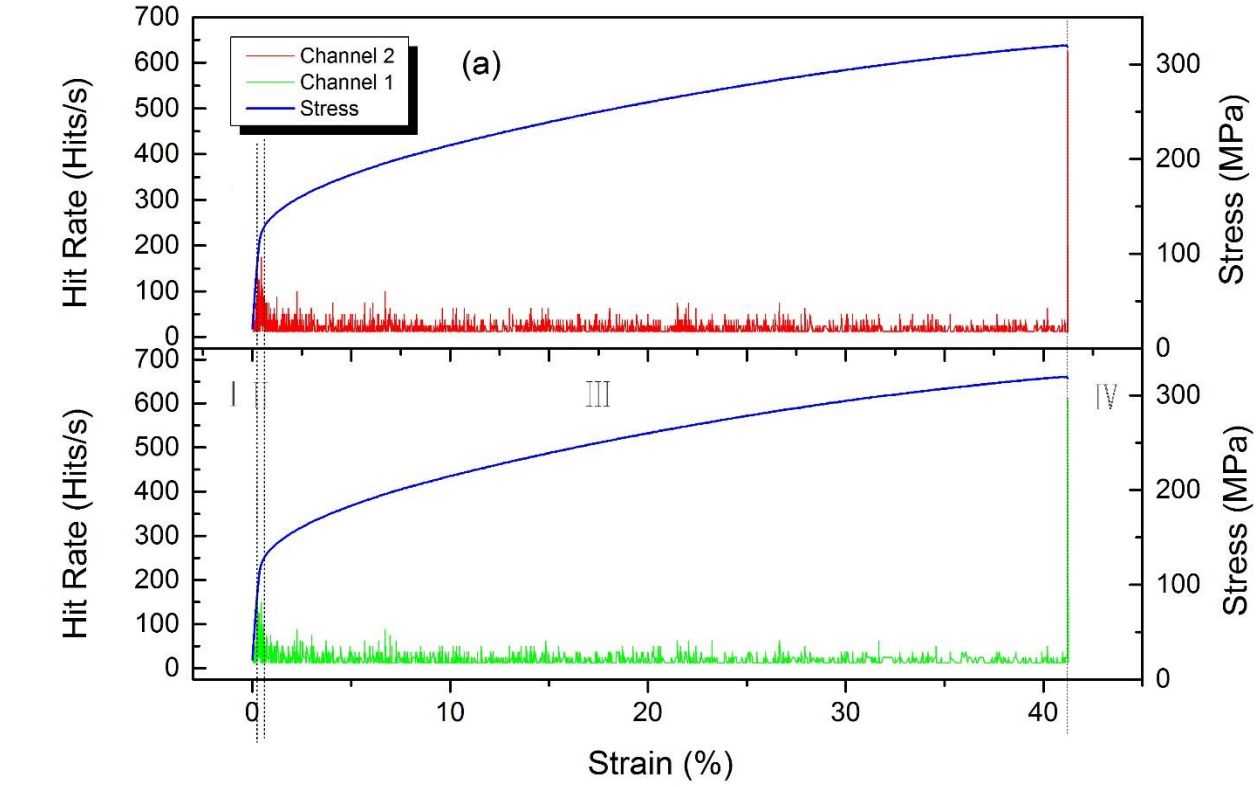
(a)
Channel 2
Channel 1
Stress
Hit Rate (Hits/s)
Stress (MPa)
I
II
III
IV
Strain (%)

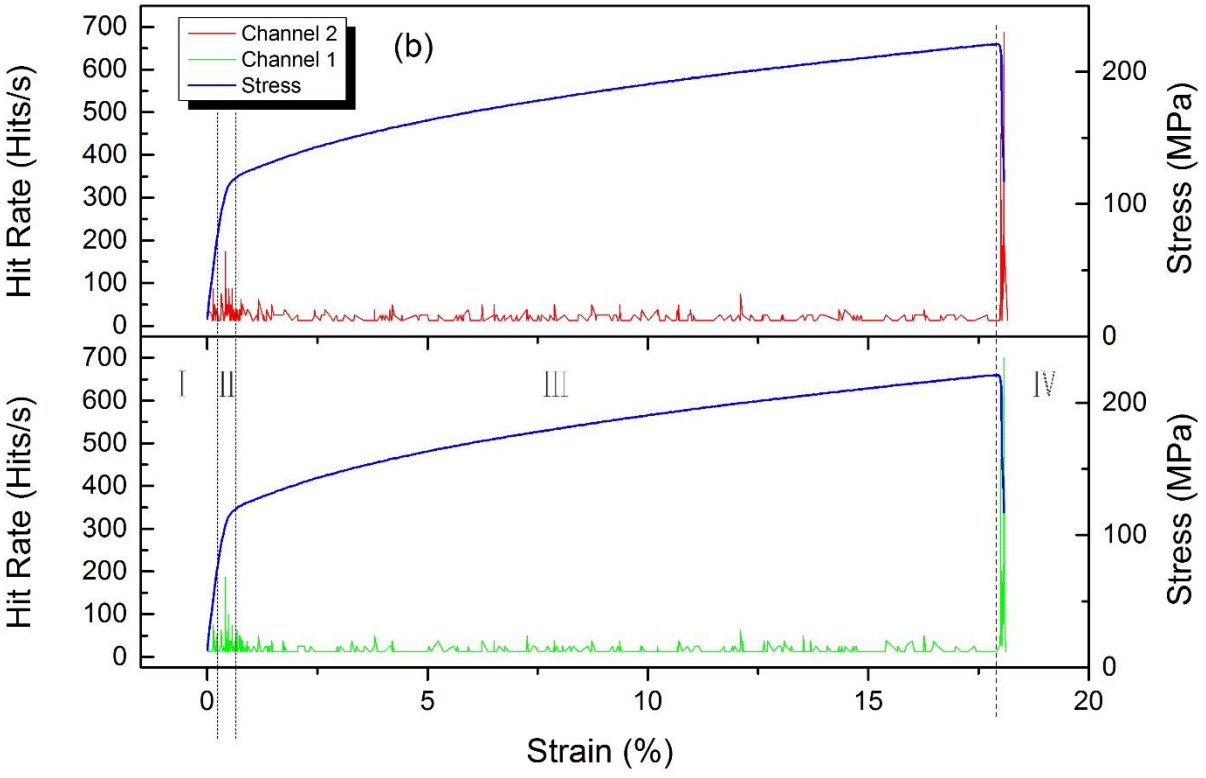
(b)
Channel 2
Channel 1
Stress
Hit Rate (Hits/s)
Stress (MPa)
I
II
III
IV
Strain (%)

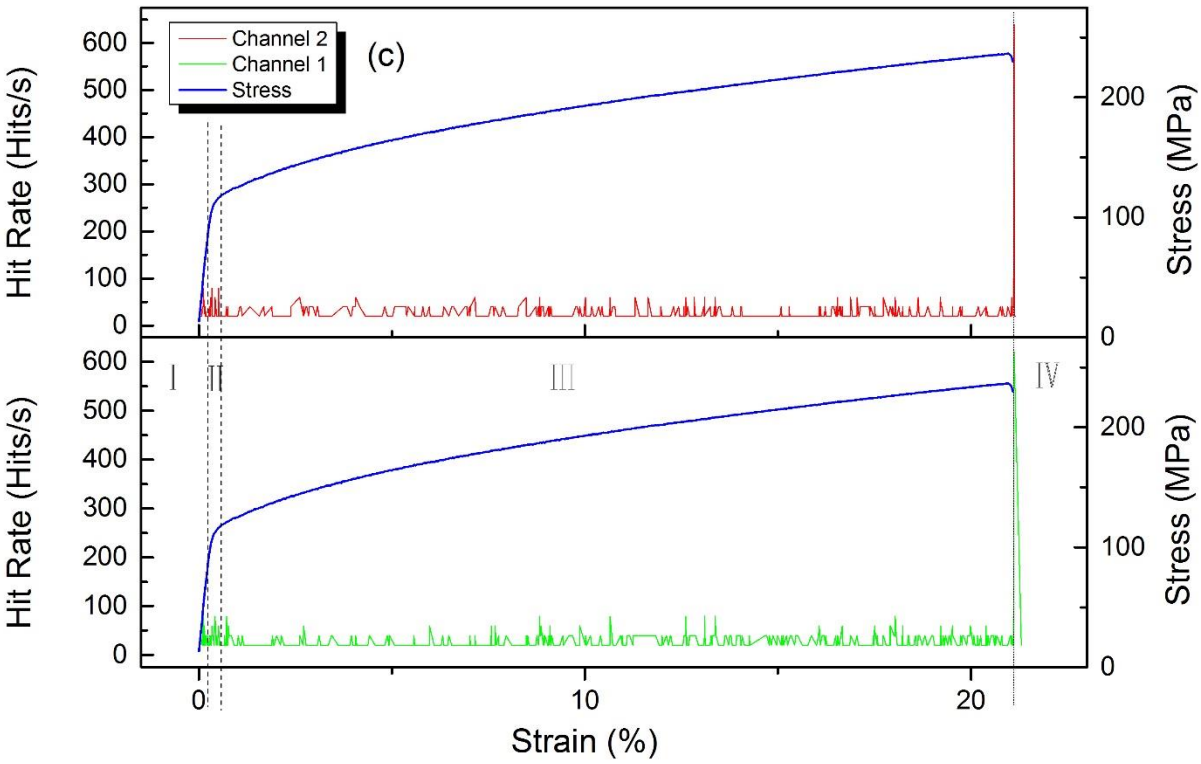
(c)
Channel 2
Channel 1
Stress
Hit Rate (Hits/s)
Stress (MPa)
I
II
III
IV
Strain (%)

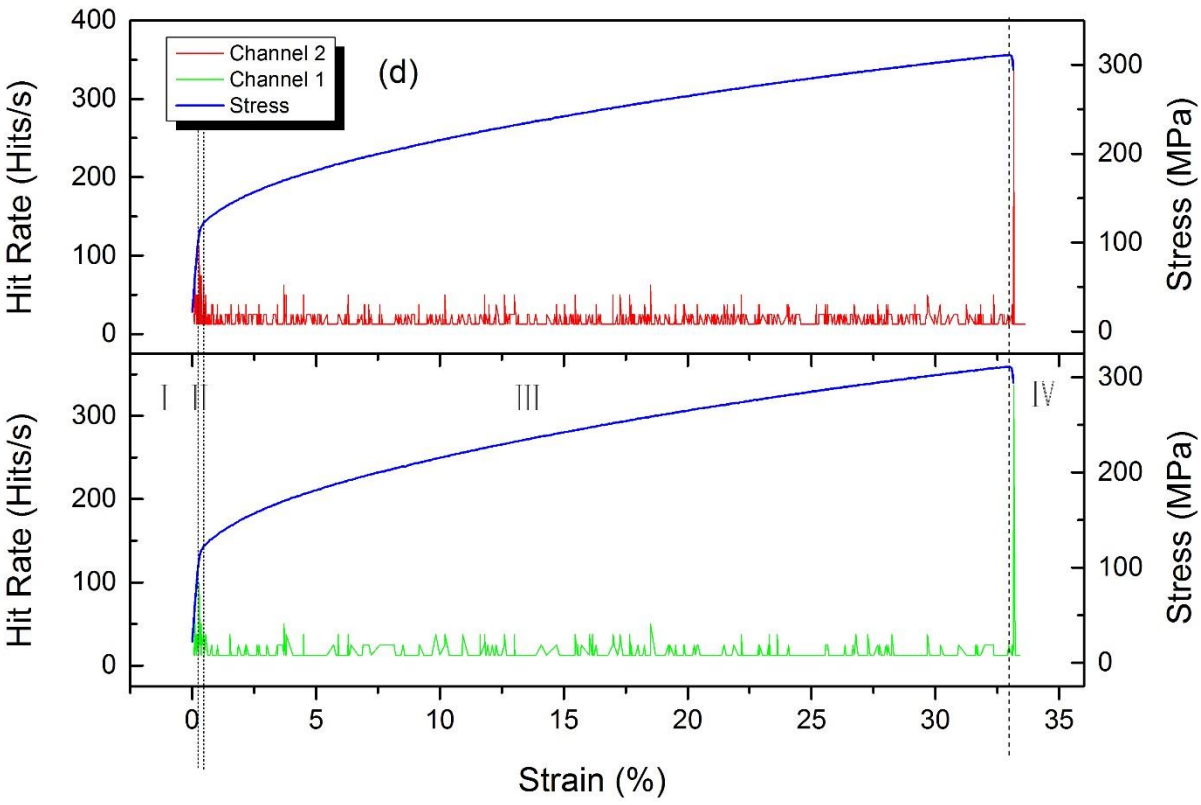
(d)
Channel 2
Channel 1
Stress
Hit Rate (Hits/s)
Stress (MPa)
I
II
III
IV
Strain (%)

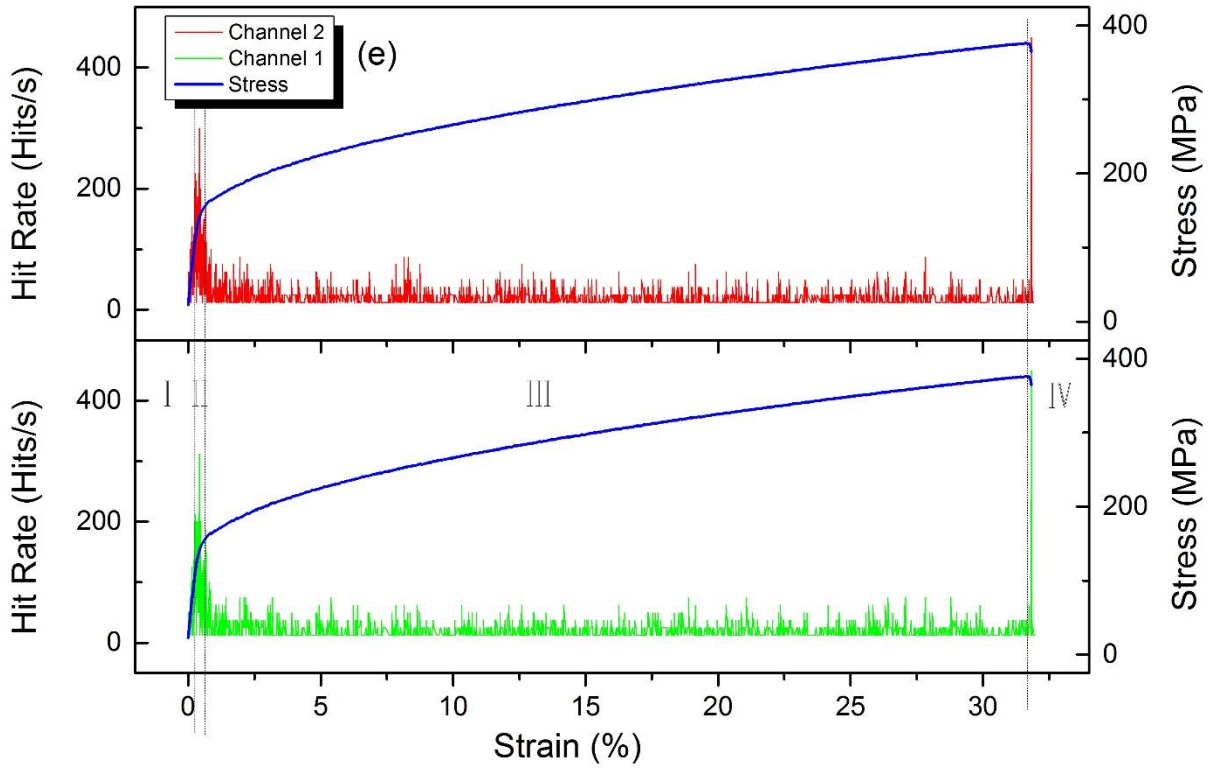

Figure 4.1 AE hit rate and stress versus strain for (a) SS 316L-1360-1; (b) SS 316L-1360-2; (c) SS 316L-1360-3; (d) SS 316L-1375-1; (e) SS 316L-1375-2; (f) SS 316L-1375-3.

By combining Figure 4.1(a)-(f) with Figure 4.2(a)-(f), it is evident that significant AE hit rate is generated in region II besides region IV, which indicates that the noticeable peak in region II is a marker of the transition from elastic deformation to plastic deformation. From Figure 4.2(a)-(f), the ranges of regions II (in strain) are 0.232-0.603%, 0.236-0.644%, 0.237-0.578%, 0.234-0.584%, 0.259-0.634% and 0.260-0.605%, respectively.

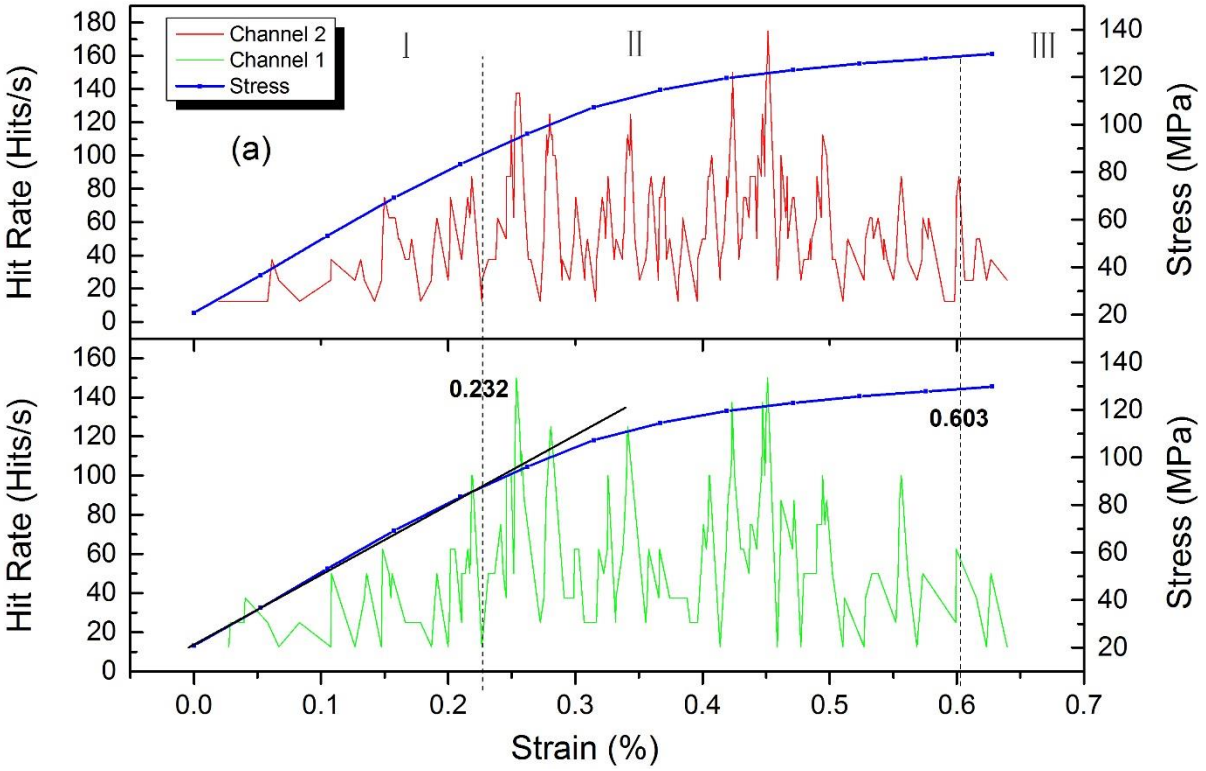
Channel 2
Channel 1
Stress
(a)
I
II
III
0.232
0.603
Hit Rate (Hits/s)
Stress (MPa)
Strain (%)

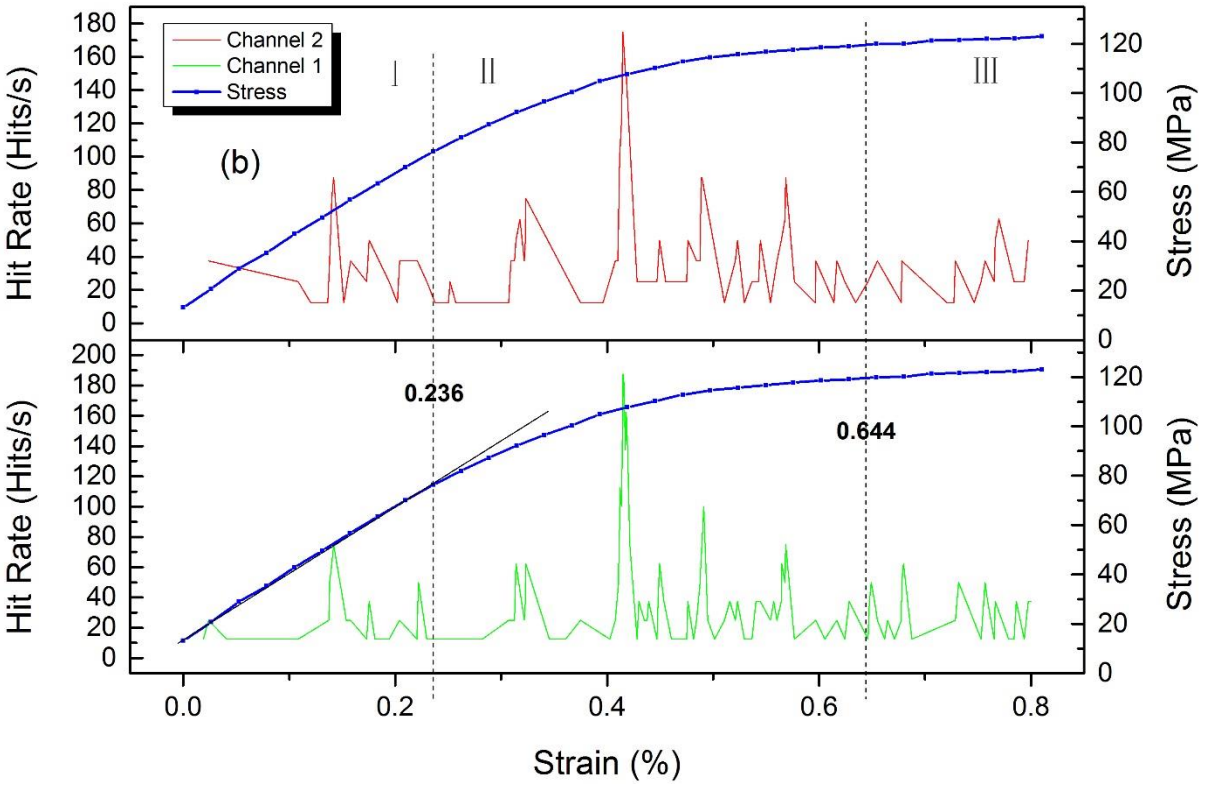
Channel 2
Channel 1
Stress
(b)
I
II
III
0.236
0.644
Hit Rate (Hits/s)
Stress (MPa)
Strain (%)

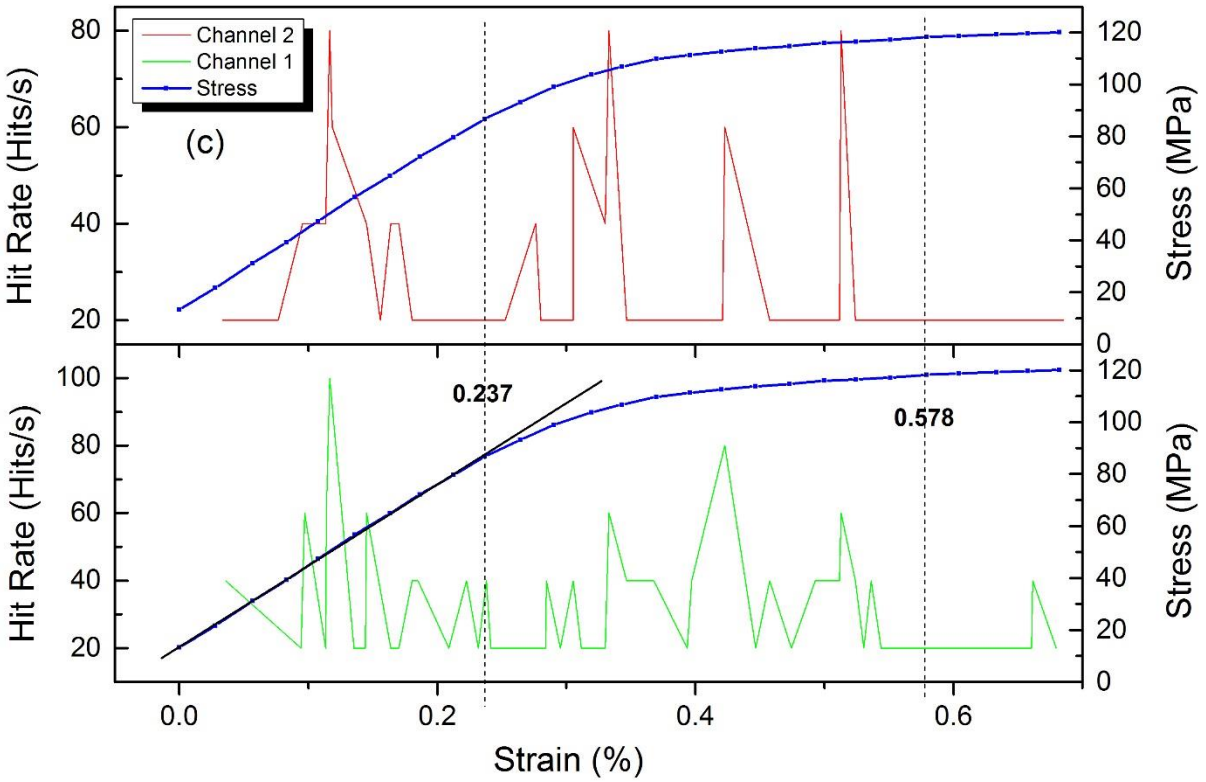
Channel 2
Channel 1
Stress
(c)
Hit Rate (Hits/s)
Stress (MPa)
0.237
0.578
Strain (%)

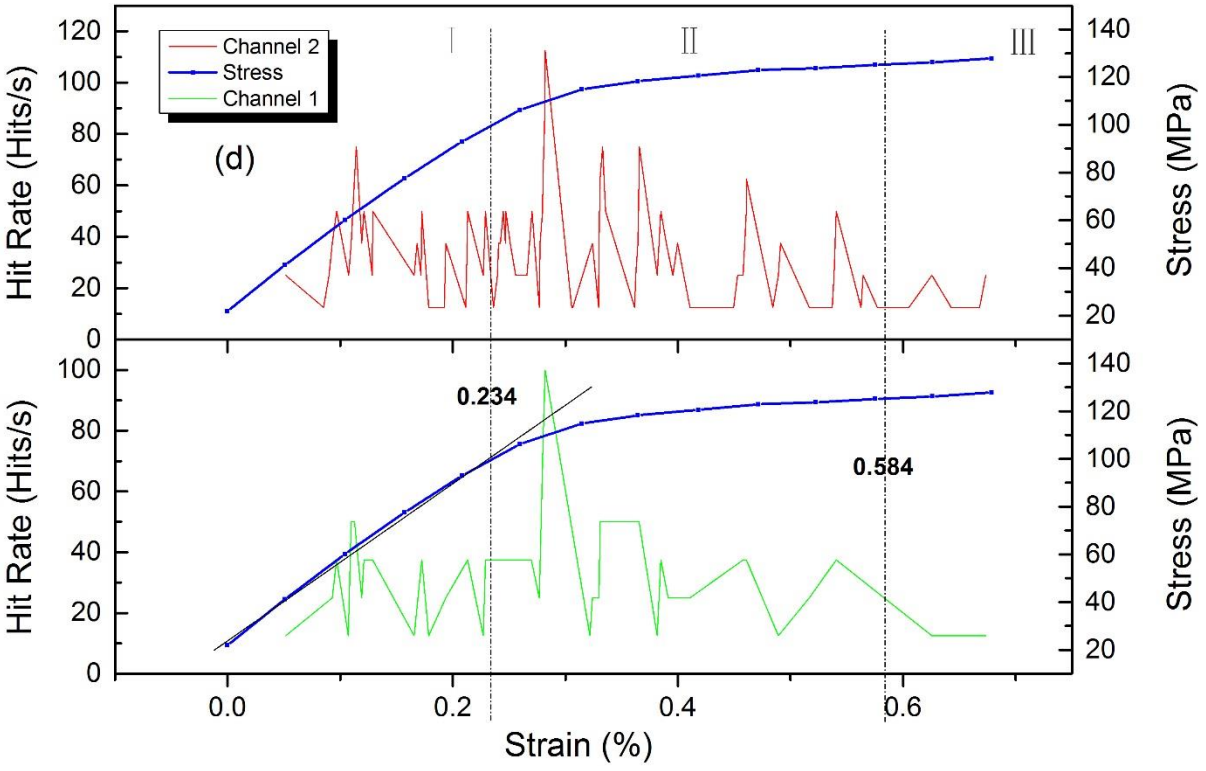
Channel 2
Stress
Channel 1
(d)
I
II
III
Hit Rate (Hits/s)
Stress (MPa)
0.234
0.584
Strain (%)

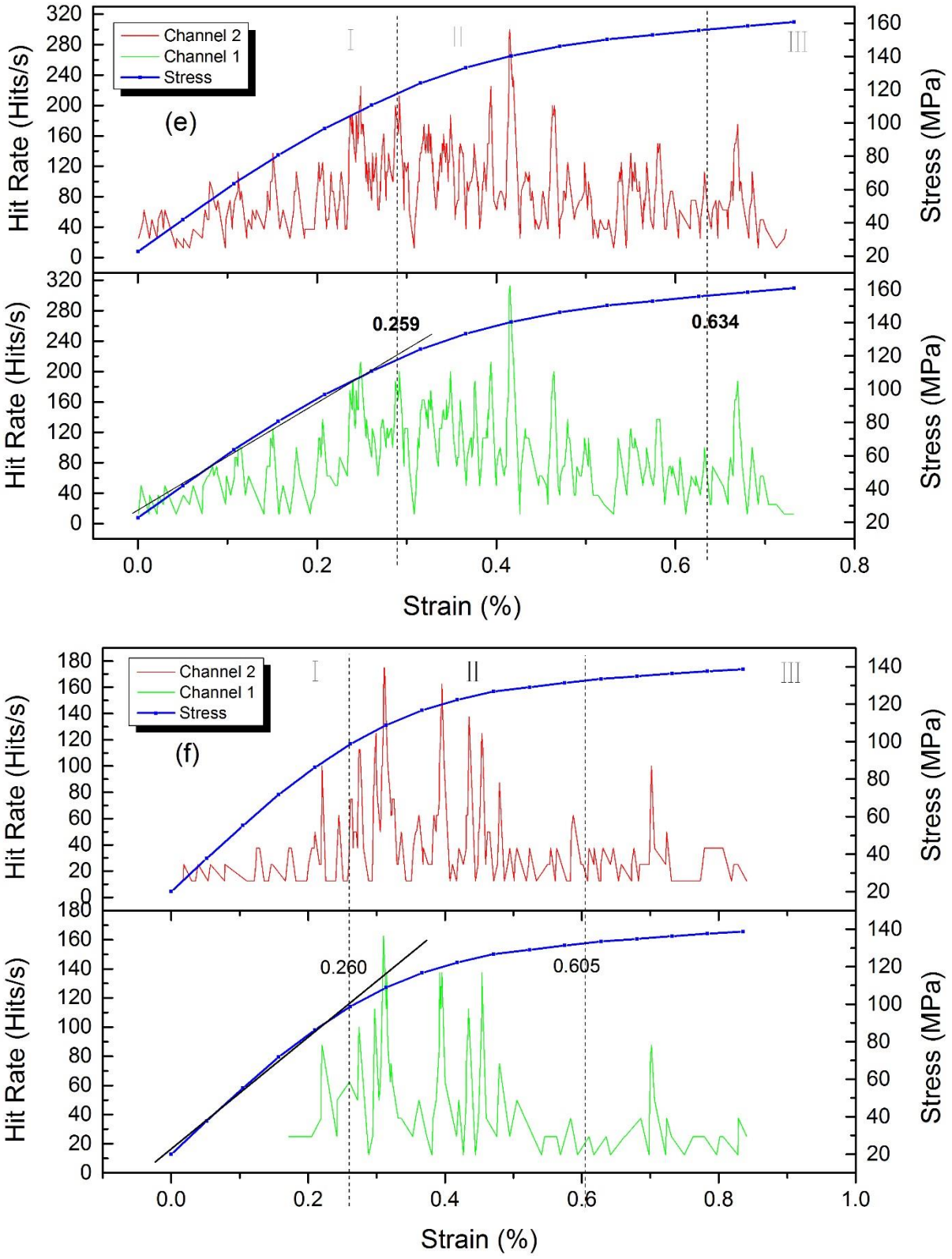

Figure 4.2 AE hit rate and stress versus strain in region I and II for (a) SS 316L-1360-1; (b) SS 316L-1360-2; (c) SS 316L-1360-3; (d) SS 316L-1375-1; (e) SS 316L-1375-2; (f) SS 316L-1375-3.

4.1.2 SS 420 Series

As SS 316L series, this series also includes two groups with 3 specimens each: one is sintered at 1360 ℃ with 90-min holding time and the other is sintered at 1375 ℃ with 90-min holding time. They are labeled as SS 420-1360-1, SS 420-1360-2, SS 420-1360-3, SS 420-1375-1, SS 420-1375-2 and SS 420-1375-3, respectively. Figure 4.3(a)-(f) represent nearly the same tendency of hit rate change: with the increase of the strain, the hit rate still rises at region I and II until reaching the climax, then it decreases, but the hit rate increases continuously after entering region III till fracture at region IV. It is noticed that there is no distinct peak in Figure 4.3 while there exist two distinct peaks in each of Figure 4.1. Significant AE hit rates appear mainly in region III and region IV.

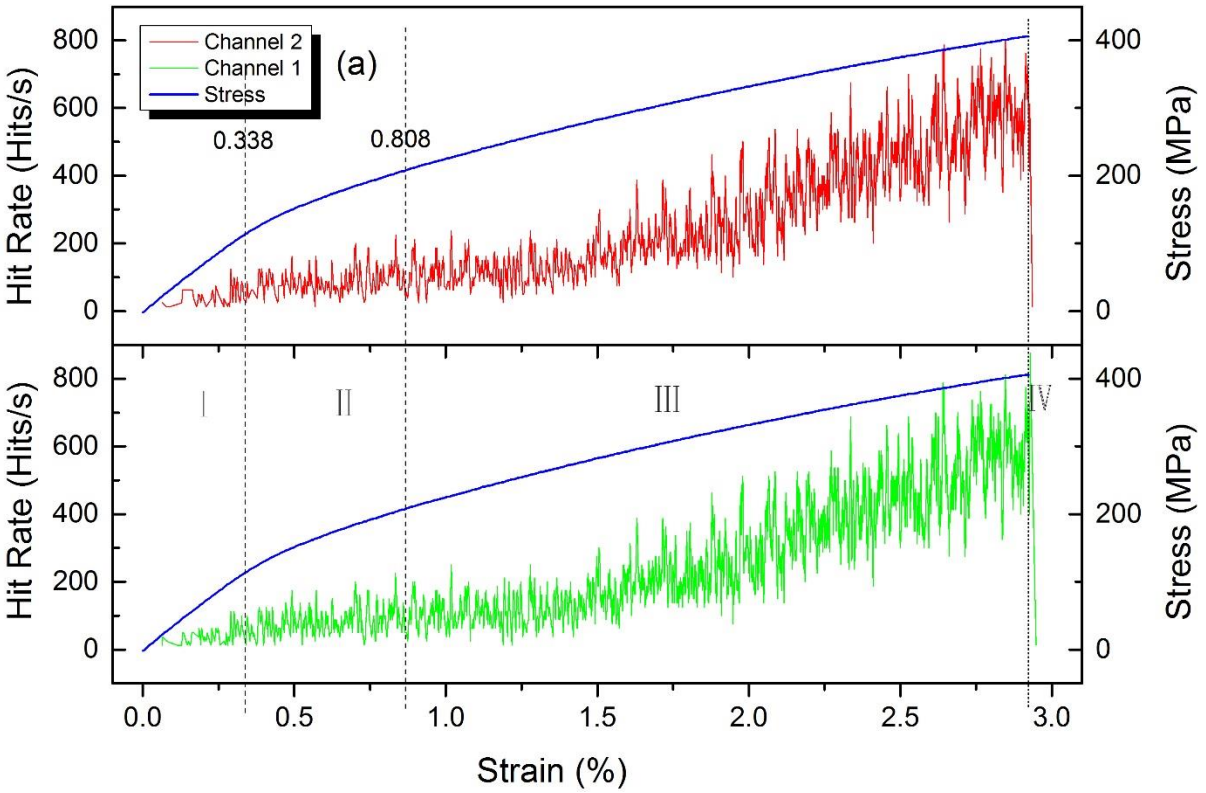

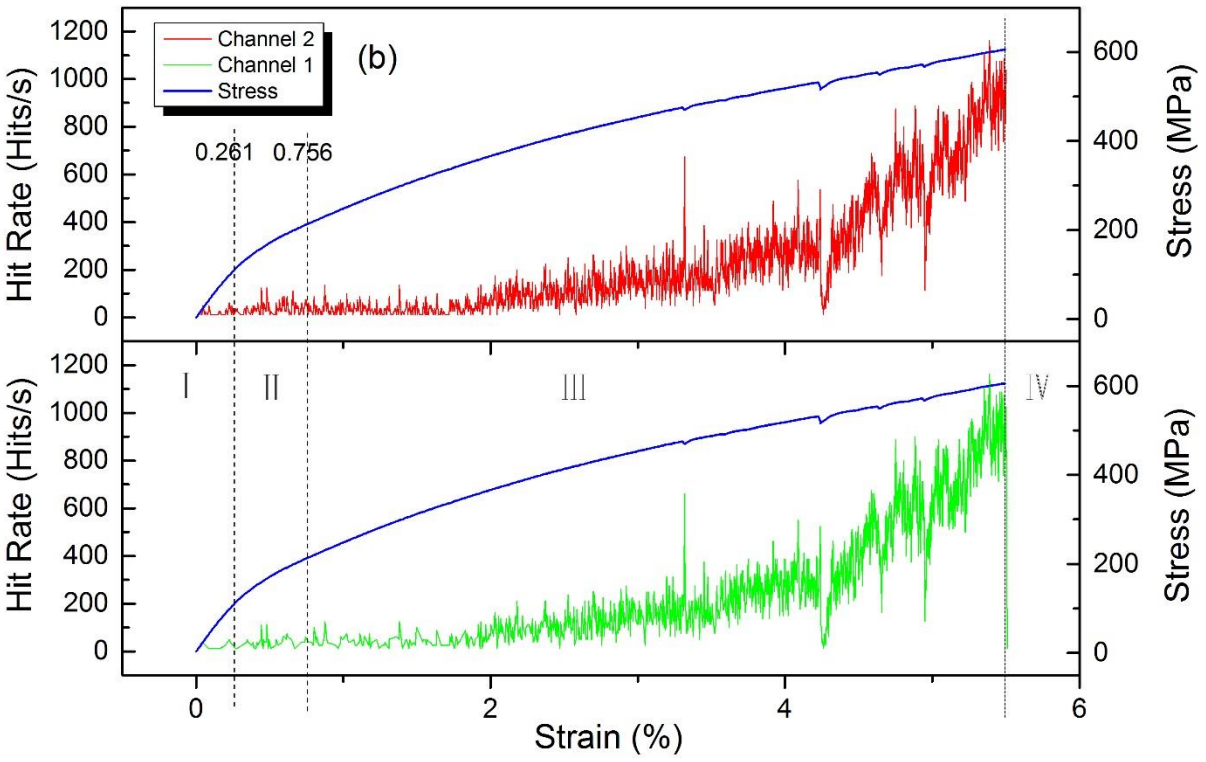
(b)
Channel 2
Channel 1
Stress
0.261
0.756
Hit Rate (Hits/s)
Stress (MPa)
I
II
III
IV
Strain (%)

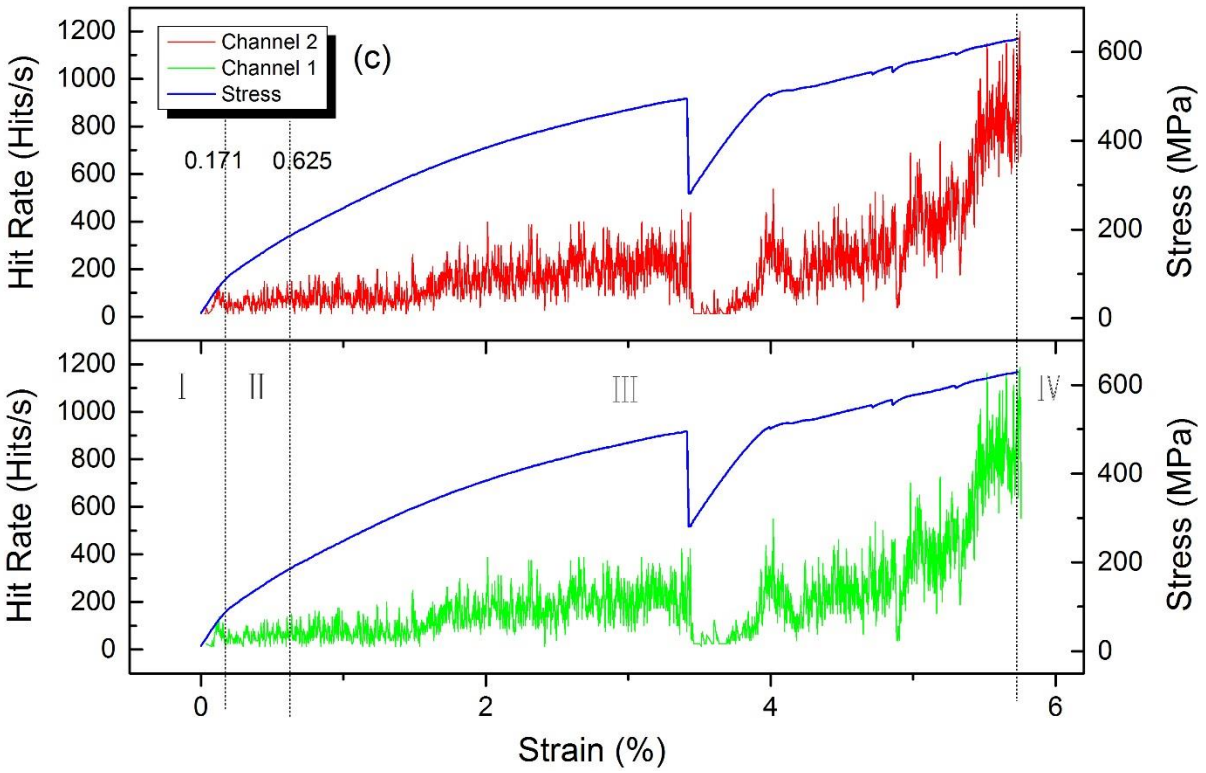
(c)
Channel 2
Channel 1
Stress
0.171
0.625
Hit Rate (Hits/s)
Stress (MPa)
I
II
III
IV
Strain (%)

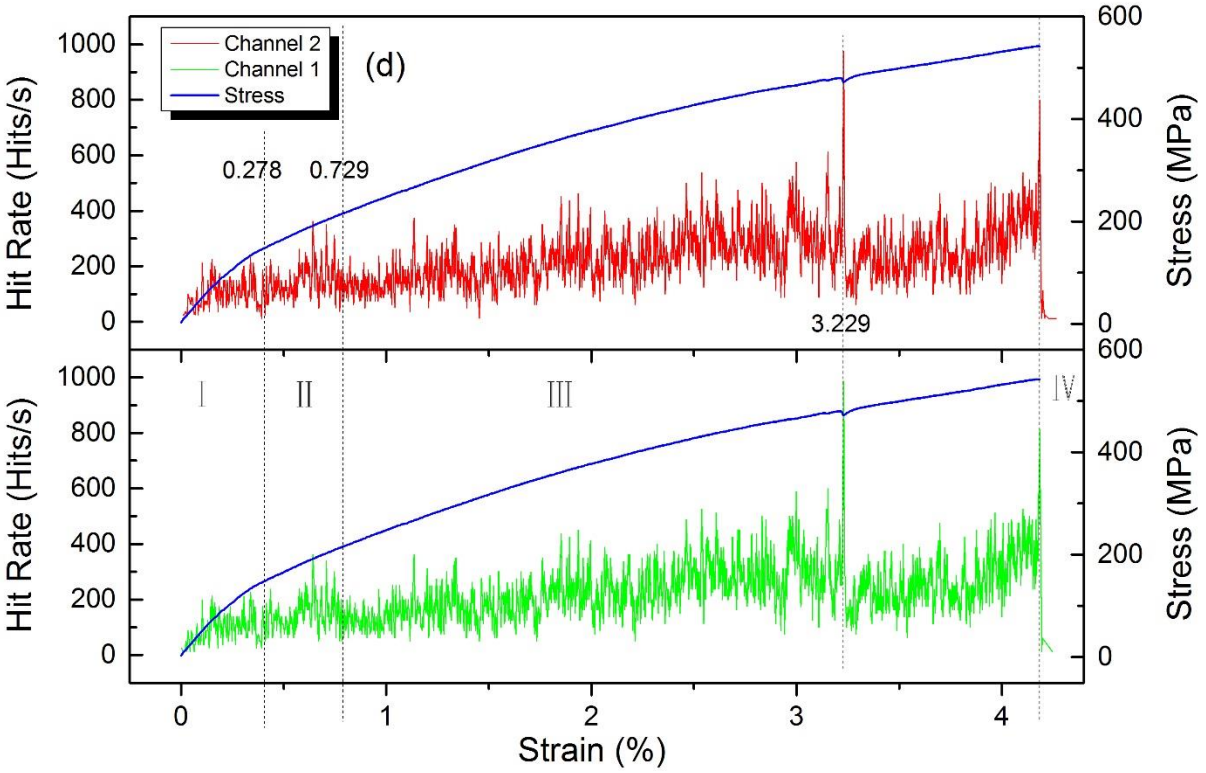
Channel 2
Channel 1
Stress
(d)
0.278
0.729
3.229
Hit Rate (Hits/s)
Stress (MPa)
I
II
III
IV
Strain (%)

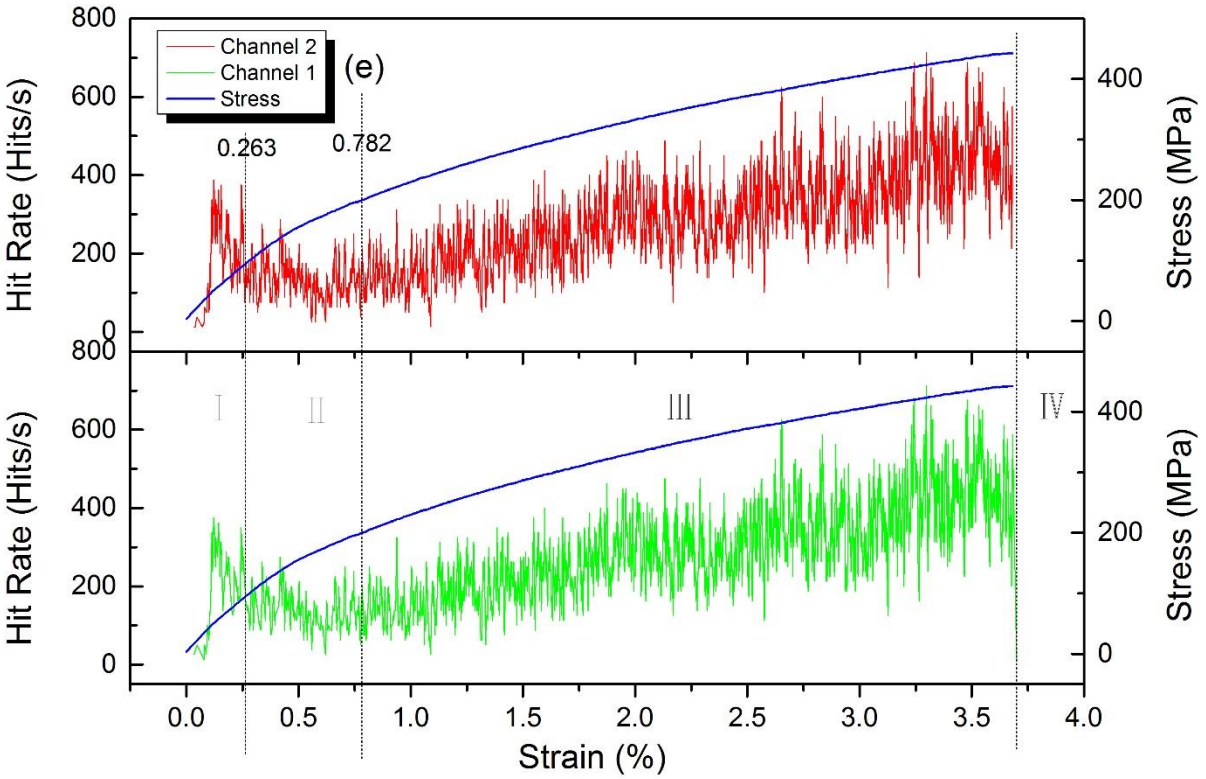
Channel 2
Channel 1
Stress
(e)
0.263
0.782
Hit Rate (Hits/s)
Stress (MPa)
I
II
III
IV
Strain (%)

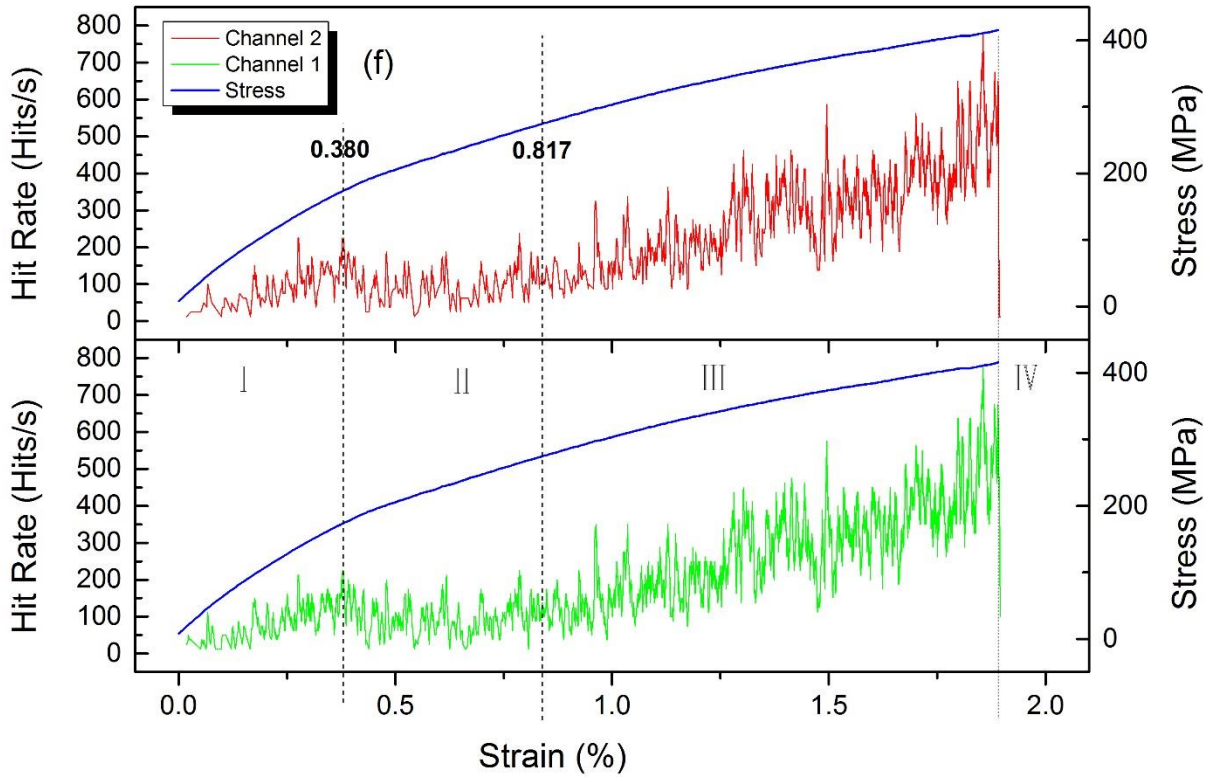

Figure 4.3 AE hit rate and stress versus strain for (a) SS 420-1360-1; (b) SS 420-1360-2; (c) SS 420-1360-3; (d) SS 420-1375-1; (e) SS 420-1375-2; (f) SS 420-1375-3.

Some interesting phenomena are discovered by combining Figure 4.3(b) with Figure 4.4(i). AE hit rate drops abruptly below 100 units even close to zero when a "pit" turns up in stress-strain curve. After that moment, the hit rate rises wavelikely. Unlike the pit 3 and pit 4 in Figure 4.4(i), it is more evident for the only pit in Figure 4.3(d) as well as pit 1 and pit 2 in Figure 4.4(i). Moreover, an AE hit rate peak is generated with the appearance of each pit. Although similar peaks accompanied with valleys are also observed, there are no pits taking place at the same strain, which demonstrates the occurrence of micro-cracks. However, a valley and a pit turning up at the same strain denotes the macro-crack is generated. If adding up a peak, the pit in stress-strain curve will be more noticeable. As is depicted in Figure 4.3(c) and Figure 4.4(ii) for SS 420-1360-3 specimen, the stress suddenly decreases dramatically and then it behaves as a new tensile test running. Generally, such great decrease of stress implies the

failure of a material. In this case, there might be some particles where dislocations accumulate right on the path of crack propagation so that the fracture is prevented after propagation of the formed macro-cracks. As for SS 420-1375-2 (see Figure 4.3(e)), the unexpected peak in region I may be caused by too much load applied at the beginning.

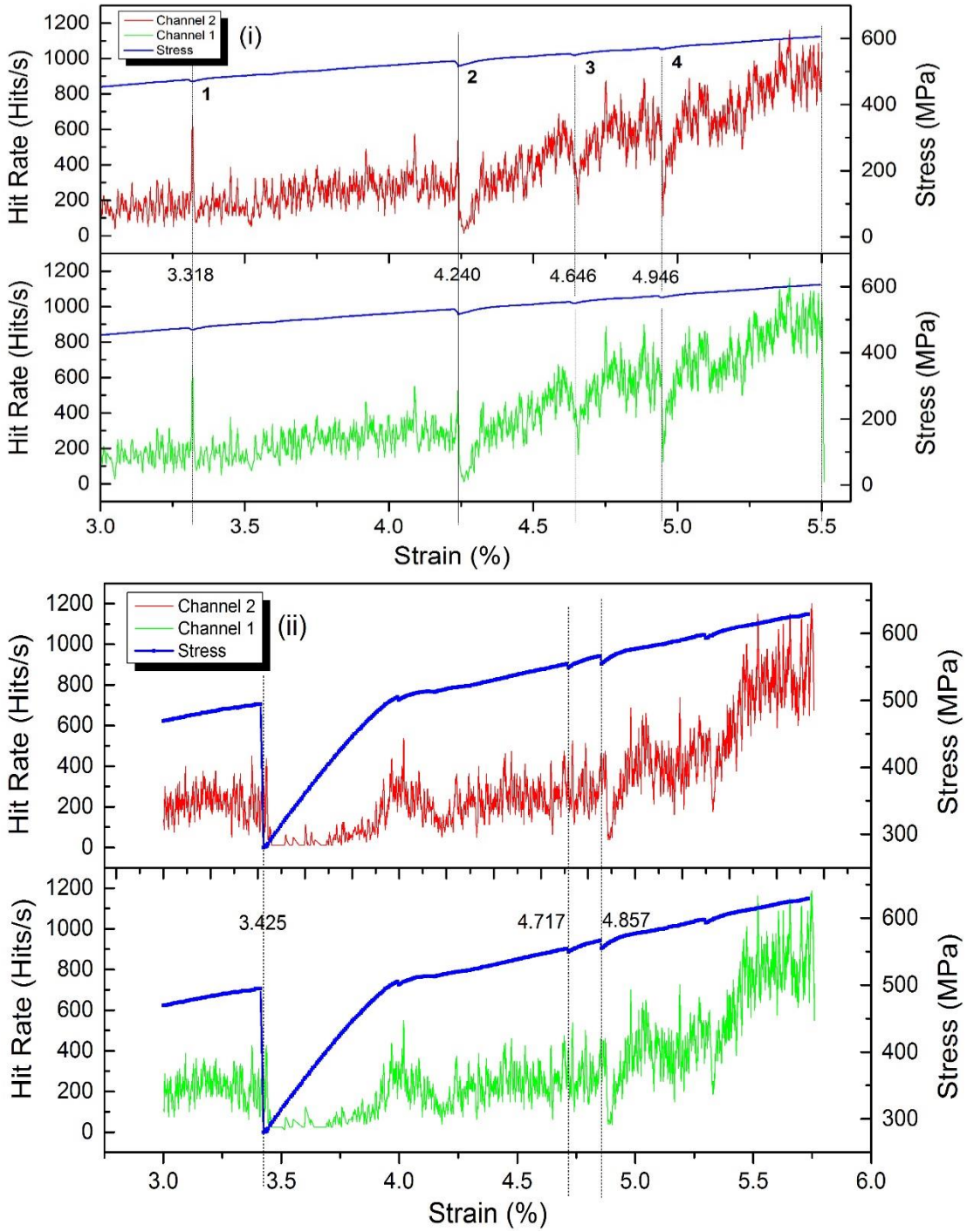

Figure 4.4 AE hit rate and stress versus strain for (i) SS 420-1360-2 in part of region III; (ii) SS 420-1360-3 in part of region III.

4.1.3 Two Fracture Modes

Two fracture modes during tensile test are summarized from Figure 4.1 and Figure 4.3: low ductility mode and high ductility mode. SS 420 series specimens belong to low ductility mode, whose strain range from 1.89% to 5.50%; while SS 316L series specimens are high ductility mode, whose strain range from 18.1% to 41.2%. As described above, the characteristic of low ductility mode is wavelikely increasing hit rate; while that of high ductility mode is two distinct peaks in region II and region IV, respectively.

Stress-strain curves for both modes lack yield points indicate that plastic events take place at lower strains, which are related to short-range dislocation motion. Due to the high dislocation density which may be produced during the manufacture or sintering process existing prior to deformation, an abundance of potential mobile dislocations is provided and mutual interactions of dislocations restrict further distance of propagation [26]. The limit distance dislocations are able to move leads to rapid multiplication from Freak-Read or grain boundary [34] with short range, resulting in micro-yielding so that they will accumulate and transform into macro-yielding smoothly when the stress is large enough, and then plastic deformation continues and the stress increases but not drop. Meanwhile, detectable AE signals are generated in region I and so are significant AE signals in region II by those short range dislocation motions. The peaks in region II for low ductile mode are inconspicuous because hit rates in region III are much larger than those in region II.

Huge differences take place from region III between high ductility mode and low ductility mode: hit rates are pretty low for the former one while hit rates rise continuously at high level

for the later. In region III, as plastic deformation rises, the specimen undergoes increasing working hardening, which leads to the increase of dislocation density. The formation of dislocation cells and dislocation tangling reduce the dislocation free path and velocity and the mobile dislocation density [19]. AE hits rate decrease obviously because single dislocation motion cannot generate detectable AE signals. For the low ductility mode, detectable AE signals are mainly produced by micro-crack propagation. Since the samples are porous inside, stress concentration commonly exists in the vicinity of each pore. In region III, stress concentration effect is stronger and stronger with increasing strain hardening, so that micro-cracks around pores are easier and easier to form and propagate, resulting in increasing detectable AE signals. Last but not the least, in region IV, high ductility mode sometimes shows necking behavior before failure, while low ductility mode always breaks at the maximum stress (UTS).

4.2 MECHANICAL PROPERTIES AND POROSITY EFFECT

Table 4.1 shows the density results measured by buoyancy method (Archimedes' principle). In each specimen, the average density differs between every two parts. For most of the specimens, those differences are quite large, indicating high inhomogeneity which might be caused by insufficient sintering. Theoretical density of SS 316L is 7.99 g/cm^3 and that of SS 420 is 7.80 g/cm^3. $\rho\% = 100*(\rho/\rho_t)$.

Table 4.1 Density of SS 316L Series and SS 420 Series Specimens

Specimen	Condition	No.	ρ(g/cm^3)					ρ%
			a	b	c	d	Total	Total
SS 316L	1360℃ 90min	1	5.86	5.94	5.89	\	5.89	73.72
		2	5.35	5.67	5.76	\	5.58	69.79
		3	6.02	5.47	5.53	\	5.71	71.45
	1375℃ 90min	1	5.01	5.88	5.48	7.38	5.88	73.61
		2	6.45	6.08	5.64	\	6.03	75.50
		3	6.67	5.99	7.27	5.05	6.11	76.49
SS 420	1360℃ 90min	1	5.73	6.12	6.17	\	5.98	76.61
		2	6.43	6.33	6.38	6.56	6.37	81.61
		3	6.55	6.40	6.43	6.51	6.42	82.33
	1375℃ 90min	1	7.38	6.58	7.67	6.81	7.04	90.24
		2	6.63	6.41	6.85	\	6.68	85.64
		3	6.04	6.66	5.71	7.10	6.27	80.44

The tensile test results are displayed in Table 4.2, where porosity equals to 100% minus ρ% in Table 4.1. Based on ASTM A276 / A276M-15 [35], 170 MPa, 485 MPa, 193 GPa, 345 MPa ,655 MPa and 200 GPa are the minimum values of yield strength and ultimate tensile strength of SS 316L and SS 420. Compared to those, specimens manufactured by ourselves are far from them. Data in Table 4.2 are depicted in Figure 4.5 and Figure 4.6. Figure 4.5(a)-(d) represent deterioration in yield strength (YS), ultimate tensile strength (UTS), Young's modulus and strain at break with the increase of porosity, respectively. SS 316L-1375-3 and SS 420-1375-3 display abnormal values of YS or UTS based on their own porosity, which needs further study to explore the reason in the future.

Table 4.2 Tensile Test Results

Speicemen	Condition	No.	YS/MPa	E/GPa	UTS/MPa	Strain at Break/%	Width of Yield Region/%	Cumulative AE Hits	Porosity/%
SS316L	1360℃ 90min	1	128.9	29.04	320.1	41.2	0.371	4437	26.28
		2	120.1	25.90	220.8	18.1	0.379	1194	30.21
		3	118.8	31.30	236.7	21.1	0.341	1117	28.55
	1375℃ 90min	1	125.4	32.61	311.3	33.3	0.350	1572	26.39
		2	160.7	30.55	375.8	32.0	0.375	4528	24.50
		3	134.9	30.31	303.5	29.1	0.345	2424	23.51
SS420	1360℃ 90min	1	199.6	33.54	405.7	2.92	0.470	9956	23.39
		2	210.8	41.42	605.6	5.50	0.495	18325	18.39
		3	185.4	44.86	628.9	5.73	0.454	18746	17.67
	1375℃ 90min	1	206.0	40.12	542.2	4.17	0.451	13870	9.76
		2	200.0	34.50	442.5	3.68	0.519	14680	14.36
		3	270.3	43.16	415.5	1.89	0.437	7972	19.56

In Figure 4.6(a), cumulative AE hits are negatively correlated with porosity. This phenomenon can be explained by the fact that AE hits are the number of crack propagations or mobile dislocations under deformation. For specimens with high ductility, most signals are generated in region III and IV, where the quantity of mobile dislocations is too small, so that most AE hits come from crack propagations. According to sintering mechanism, pores would become smaller and smaller, even disappeared due to growth of surrounding particles or meet other moving pores and form a larger pores during sintering process. In this case, the negative correlation implies that the number of pores decreases with increasing porosity. Thus there are large pores with small quantity in the specimens with higher porosity, while small pores with large quantity exist in the specimens with lower porosity. From Figure 4.6(b), it is evident that cumulative AE hits has positive correlation with width of yield region. For SS 316L series samples (high ductility mode), the values of their width of yield region fall in the range 0.341-0.379%; while for SS 420 series samples (low ductility mode), the ones fall in the range 0.437-0.519%. It may be useful to apply these two ranges in determining which mode a material belongs to.

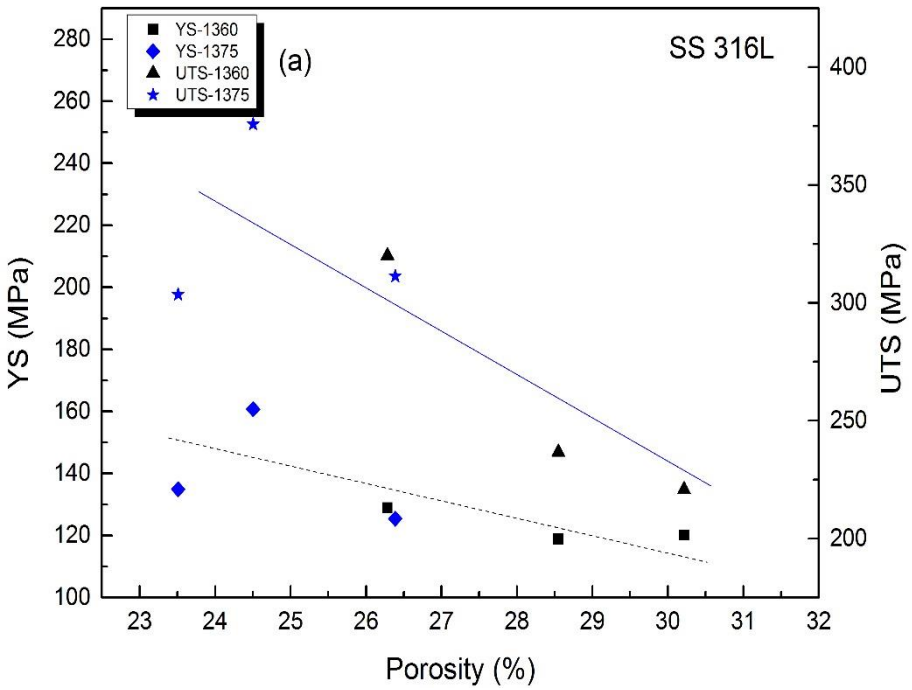
YS-1360
YS-1375
UTS-1360
UTS-1375
(a)
SS 316L
YS (MPa)
UTS (MPa)
Porosity (%)

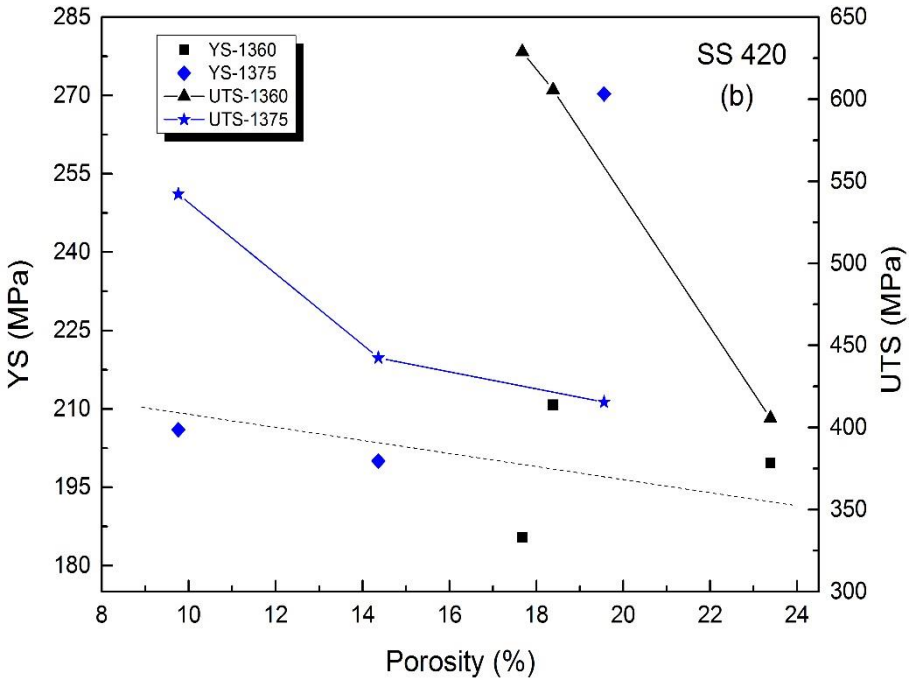
YS-1360
YS-1375
UTS-1360
UTS-1375
SS 420
(b)
YS (MPa)
UTS (MPa)
Porosity (%)

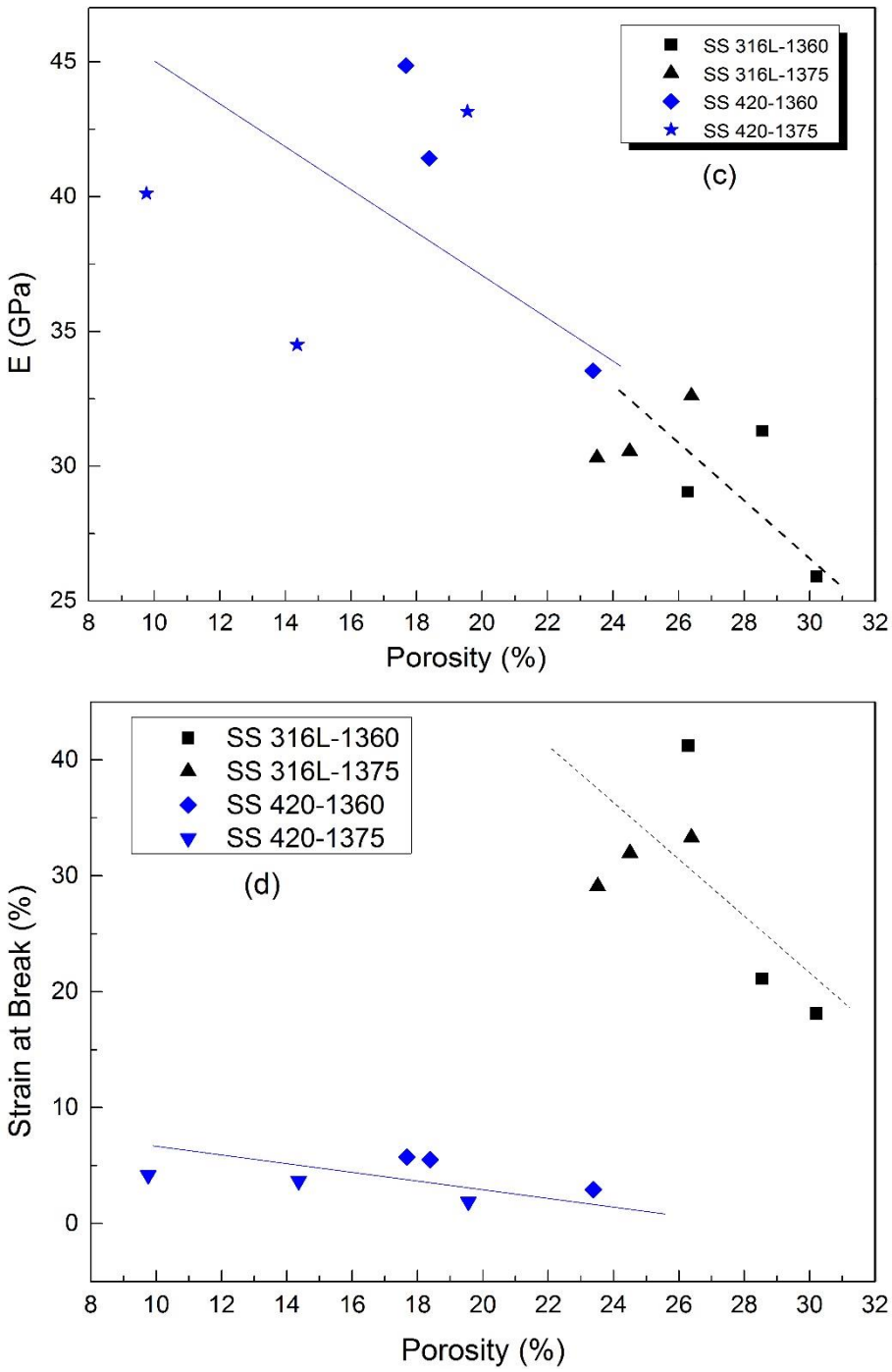

Figure 4.5 Mechanical properties versus porosity: (a) YS and UTS for SS 316L; (b) YS and UTS for SS 420; (c) Young's Modulus; (d) Strain at break.

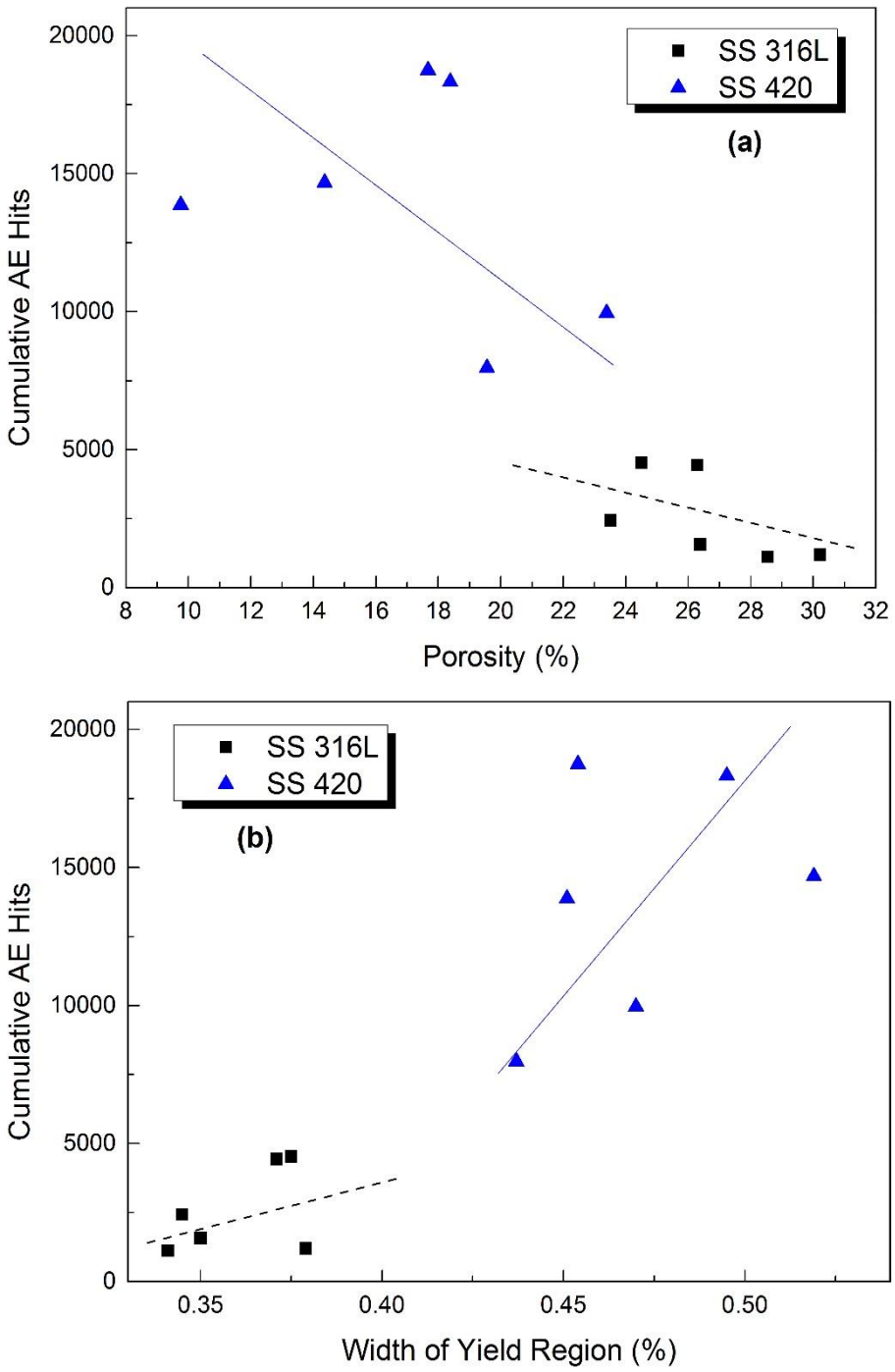

Figure 4.6 Cumulative AE hits versus (a) porosity and (b) width of yield region.

4.3 HARDNESS

The results of Vickers hardness of all the specimens can be seen in Table 4.3, where SD is abbreviation of standard deviation. The maximum standard deviation is 92.84 and the minimum one is 15.61, which are both quite large, indicating that the samples are severe inhomogenous. Generally, Vickers hardness (HV) of SS 316L is 150-600 and that of SS 420 is above 500. Compared to this criteria, our specimens are close to wrought stainless steel bars in hardness.

Table 4.3 Vickers Hardness of all the specimens

Speicemen	Condition	No.	Avg. HV	SD
SS316L	1360℃ 90min	1	197.59	42.33
		2	129.54	15.61
		3	193.10	37.27
	1375℃ 90min	1	158.82	43.05
		2	131.96	29.67
		3	164.90	21.11
SS420	1360℃ 90min	1	645.86	87.47
		2	633.38	92.84
		3	691.14	87.96
	1375℃ 90min	1	570.89	56.40
		2	588.77	37.38
		3	583.55	68.44

The main phases of our specimens are the same as standard ones. Standard SS 316L is austenitic steel and standard SS 420 is martensitic steel and. According to Table 3.1, SS 316L contains high concentration of Cr and Ni and low carbon concentration, which leads to the martensite start temperature below 0 ℃ and prevents austenite from breaking down during cooling process, even at our low cooling rate (3 ℃/min). For SS 420 series, the following is evidence which supports my opinion: hardness of lath martensite is normally HV 600-800 and

the picture (see Figure 4.7) taken by optical microscope displays the characteristics of lath martensite. The high concentration of C, Cr and Ni prevents the breakdown of austenite until martensitic transformation starts at our low cooling rate (3 ℃/min).

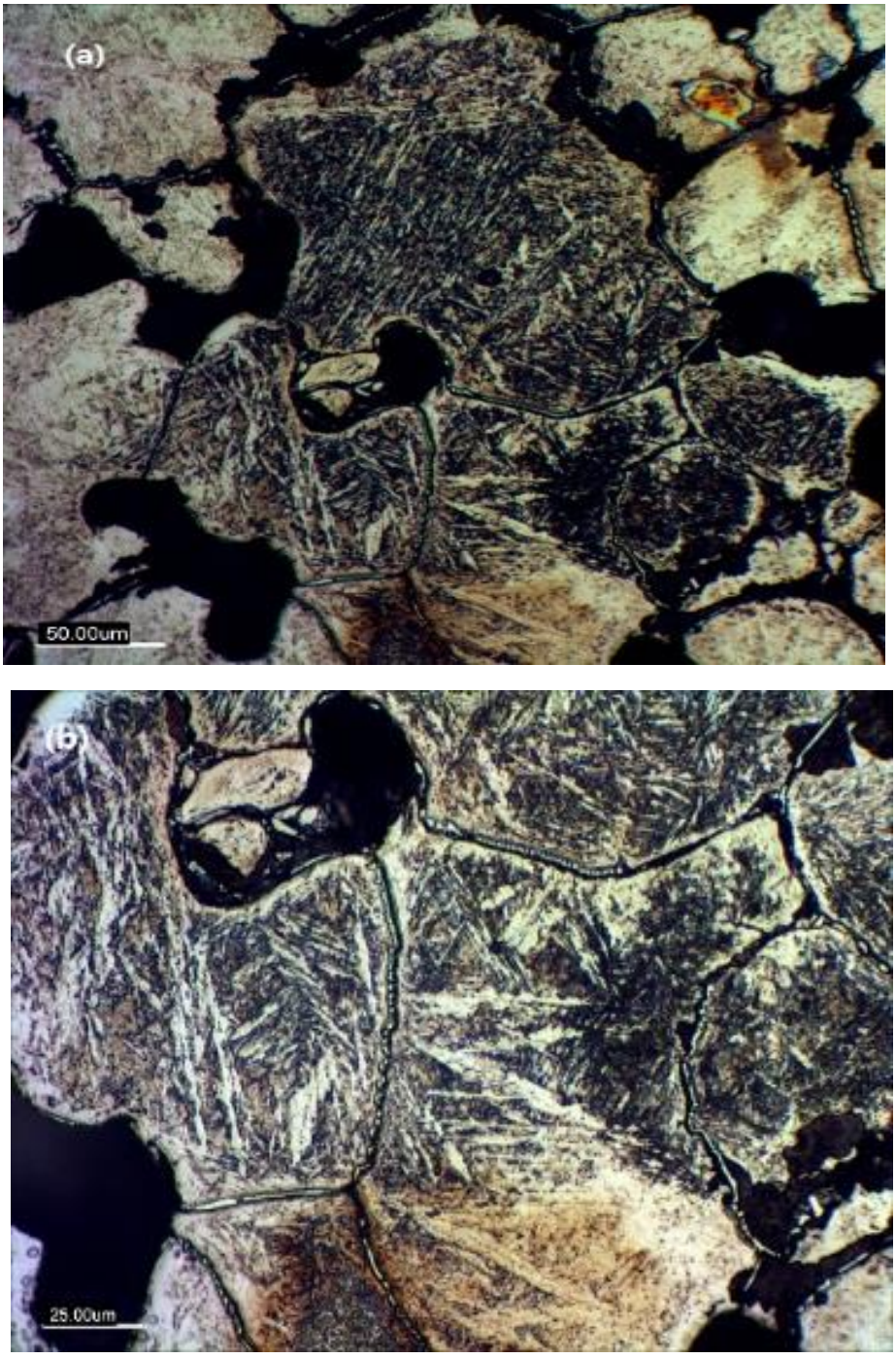

Figure 4.7 Microstructure of SS 420-1360-2 (a) 400x (b) 800x

5.0 CONCLUSIONS AND FUTURE WORKS

5.1 CONCLUSIONS

This research focused on acoustic emission evaluation and mechanical property characterization. The first part is correlating AE data with tensile test data. The second part includes tensile test, buoyancy method and hardness test, which measured a series of mechanical properties, such as yield strength (YS), Young's modulus and Vickers hardness. All the 12 specimens (tensile bars with 2 inches gauge length) were fabricated by powder based 3D-printer and then underwent sintering.

In the first part, tensile tests accompanied by acoustic emission were performed. AE hit rates versus strain for channel 1 and channel 2 are highly consistent, furthermore, their change tendency and feature events are the same. Also, two modes of fracture were discovered: high ductility mode and low ductility mode, which would be helpful to determine whether the ductility of a material is high ($\geq$ 18.1%) or low ($\leq$. 5.73%). Moreover, for the high ductility mode, the peak in yield region can be regarded as the indicator of yield beginning.

In the second part, porosity and mechanical properties were characterized, including yield strength, ultimate tensile strength, Young's modulus, strain at break, width of yield region and Vickers hardness. Compared to standard materials, our specimens are far from those in mechanical properties except for Vickers hardness. The main reason is porosity negative effect on mechanical properties. Porosity also has negative correlation with AE cumulative hits, while width of yield region is on the contrary.

5.2 FUTURE WORKS

The present research is the first step to evaluate products manufactured by 3D printer using acoustic emission technology. A few recommendations for future works as follow:

1. Establish relationship between packing density after curing and density after sintering, which will be helpful to improve product density.
2. More samples need studied to determine whether the two modes is material dependent or mechanism dependent. If they are material independent and mechanism dependent, they would be criteria to evaluate ductility.
3. The abnormal phenomena discovered in this research highly demand further study with appropriate methods.

BIBLIOGRAPHY

[1] T. F. Drouillard, " A history of acoustic emission," *Journal of Acoustic Emission,* vol. 14, pp. 1-34, 1996.

[2] "Standard Terminology for Nondestructive Examinations," in *ASTM E1316-13d*, ed. ASTM International: ASTM International, 2013.

[3] M. O. Christian U. Grosse, *Acoustic Emission Testing*. Heidelberg: Springer, 2008.

[4] C. B. Scruby, "An Introduction to Acoustic Emission," *Journal of Physics E: Scientific Instruments,* vol. 20, pp. 946-953, 1987.

[5] K. Ito and M. Enoki, "Acquisition and Analysis of Continuous Acoustic Emission Waveform for Classification of Damage Sources in Ceramic Fiber Mat," *Materials Transactions,* vol. 48, pp. 1221-1226, 2007.

[6] H. Vallen. (2002). *AE Testing Fundamentals, Equipment, Applications*. Available: http://www.ndt.net/article/v07n09/05/05.htm

[7] C. B. Scruby, G. R. Baldwin, and K. A. Stacey, "Characterisation of fatigue crack extension by quantitative acoustic emission," *International Journal of Fracture,* vol. 28, pp. 201-222, 1985.

[8] J. Kaiser, "An investigation into the occurrence of noises in tensile tests, or a study of acoustic phenomena in tensile tests," Doctor of Philosophy, Technical University of Munich, Munich, Germany, 1950.

[9] W. T. Lauten, A. Tahini, and M. Khan, "Application of the Kaiser effect to the measurement of in-situ stresses in Arabian devonian sandstone," presented at the The Society of Core Analysts Symposium Edinburgh, Scotland, 2001.

[10] T. J. Fowler, "Acoustic Emission Testing of Fiber Reinforced Plates," presented at the ASCE Fall Convention, San Francisco, California, October 17-21, 1977.

[11] NDT.net. *Introduction to Acoustic Emission Testing - Equipment*. Available: https://www.nde-ed.org/EducationResources/CommunityCollege/Other%20Methods/AE/AE_Equipment.htm

[12] NDT.net. *Introduction to Acoustic Emission Testing - Introduction*. Available: https://www.nde-ed.org/EducationResources/CommunityCollege/Other%20Methods/AE/AE_Intro.htm

[13] L. Sun and Y. Li, "Acoustic emission sound source localization for crack in the pipeline," presented at the Chinese Control and Decision Conference (CCDC), Xuzhou, China, 2010.

[14] R. K. Miller, E. v. K. Hill, and P. O. Moore, Eds., *Acoustic Emission Testing* (Nondestructive Testing Handbook 5). Columbus, OH: The American Society for nondestructive Testing, 2005, p.^pp. Pages.

[15] J. Xu, G. Lacidogna, and C. Alberto, "Accuracy of Acoustic Emission Localization for Masonry Structures Monitoring," in *The 13th International Conference on Fracture*, Beijing, China, 2013.

[16] S. K. F. Ansel C. Ugural, *Advanced Strength and Applied Elasticity*, 4th ed. New Jersey: Prentice Hall, 2003.

[17] D. Amitrano, "Brittle-ductile transition and associated seismicity: Experimental and numerical studies and relationship with the b value," *Journal of Geophysical Research-Solid Earth*, vol. 108, Jan 25 2003.

[18] V. Moorthy, T. Jayakumar, and B. Raj, "Acoustic emission technique for detecting micro-and macroyielding in solution-annealed AISI Type 316 austenitic stainless steel," *International journal of pressure vessels and piping*, vol. 64, pp. 161-168, 1995.

[19] Z. Y. Han, H. Y. Luo, and H. W. Wang, "Effects of strain rate and notch on acoustic emission during the tensile deformation of a discontinuous yielding material," *Materials Science and Engineering a-Structural Materials Properties Microstructure and Processing*, vol. 528, pp. 4372-4380, May 24 2011.

[20] P. Johan Singh, C. Mukhopadhyay, T. Jayakumar, S. Mannan, and B. Raj, "Understanding fatigue crack propagation in AISI 316 (N) weld using Elber's crack closure concept: Experimental results from GCMOD and acoustic emission techniques," *International Journal of Fatigue*, vol. 29, pp. 2170-2179, 2007.

[21] C. Mukhopadhyay, K. Ray, T. Jayakumar, and B. Raj, "Acoustic emission from tensile deformation of unnotched and notched specimens of AISI type 304 stainless steels," *Materials Science and Engineering: A*, vol. 255, pp. 98-106, 1998.

[22] *Acoustic Emission, Special Technical Publication 505*. Baltimore: American Society for Testing and Materials, 1972.

[23] G. E. Dieter and D. Bacon, *Mechanical metallurgy* vol. 3: McGraw-Hill New York, 1986.

[24] Wikipedia. *Tensile Testing*. Available: http://en.wikipedia.org/wiki/Tensile_testing

[25] "Standard Test Methods for Tension Testing of Metallic Materials," in *ASTM E8/E8M-13a*, ed. West Conshohocken, PA: ASTM International, 2013.

[26] H. N. G. Wadley and C. B. Scruby, "Cooling Rate Effects on Acoustic Emission-Microstructure Relationships in Ferritic Steels," *Journal of Materials Science,* vol. 26, pp. 5777-5792, Nov 1 1991.

[27] R. L. Smith and G. E. Sandland, "An Accurate Method of Determining the Hardness of Metals, with Particular Reference to Those of a High Degree of Hardness," *Proceedings of the Institution of Mechanical Engineers,* vol. I, pp. 623–641, 1922.

[28] "Standard Test Method for Knoop and Vickers Hardness of Materials," in *ASTM E384-11e1*, ed. West Conshohocken, PA: ASTM International, 2011.

[29] R. Noorani, *Rapid prototyping: principles and applications*. New Jersey: John Wiely & Sons, 2006.

[30] K. V. Wong and A. Hernandez, "A review of additive manufacturing," *ISRN Mechanical Engineering*, vol. 2012, 2012.

[31] E. Sachs, M. Cima, P. Williams, D. Brancazio, and J. Cornie, "Three dimensional printing: rapid tooling and prototypes directly from a CAD model," *Journal of Manufacturing Science and Engineering*, vol. 114, pp. 481-488, 1992.

[32] J.-P. Kruth, "Material incress manufacturing by rapid prototyping techniques," *CIRP Annals-Manufacturing Technology,* vol. 40, pp. 603-614, 1991.

[33] J. McDaniel, "Prometal Rapid Manufacturing," presented at the CTMA, 2005.

[34] C. B. Scruby and H. N. G. Wadley, "Tempering Effects on Acoustic-Emission Microstructural Relationships in Ferritic Steels," *Journal of Materials Science,* vol. 28, pp. 2501-2516, May 1 1993.

[35] "Standard Specification for Stainless Steel Bars and Shapes," in *ASTM A276 / A276M-15*, ed. West Conshohocken, PA: ASTM International, 2015.